The Thermodynamic Structure of the Cumulus Sub-Cloud Layer

By

Frank J. Dugan

Department of Atmospheric Science
Colorado State University
Fort Collins, Colorado

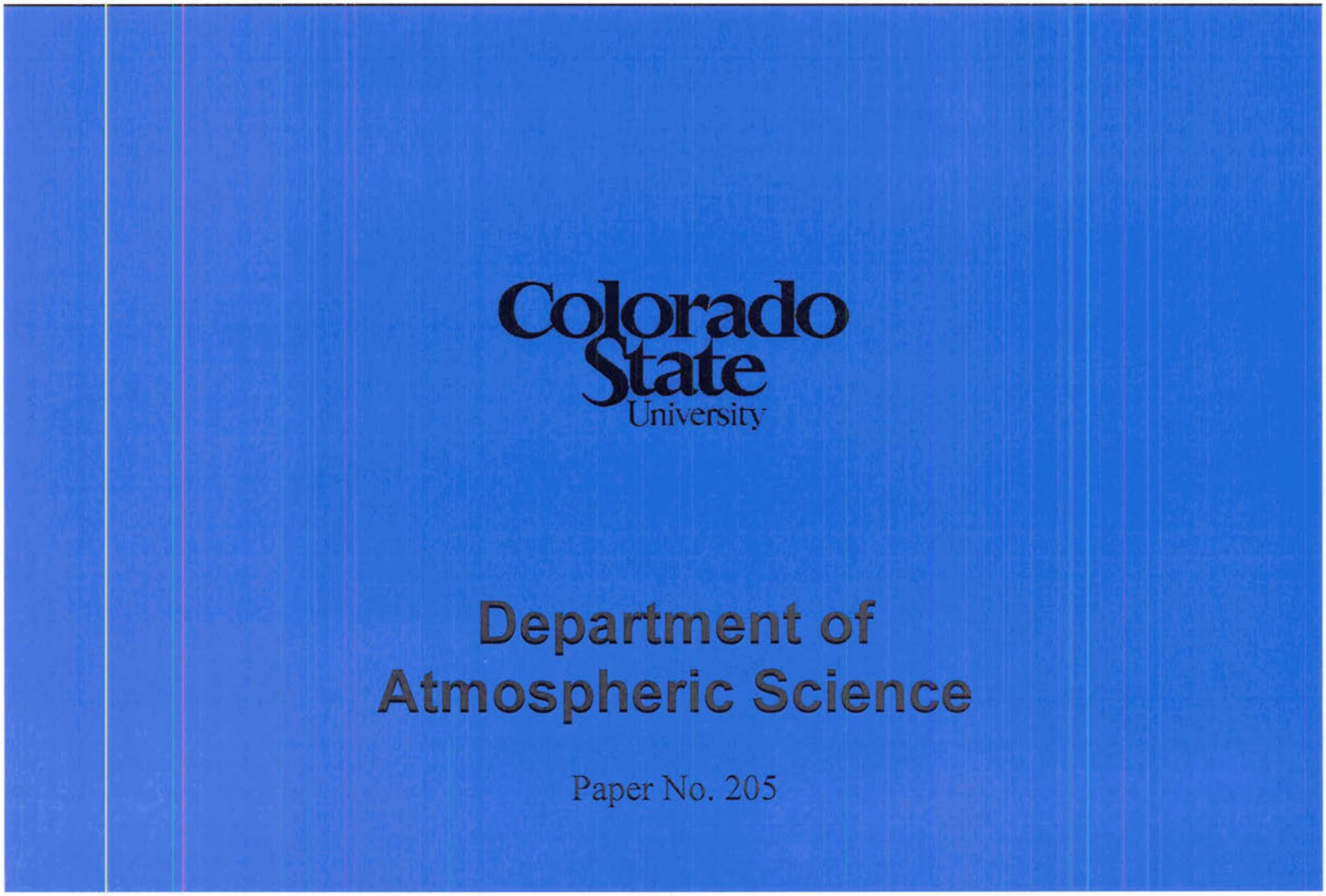

THE THERMODYNAMIC STRUCTURE OF THE CUMULUS SUB-CLOUD LAYER

by

Frank J. Dugan

Preparation of this report
has been supported by
NSF Grant GA-33182

Principal Investigator: A. K. Betts

Department of Atmospheric Science
Colorado State University
Fort Collins, Colorado
August 1973

Atmospheric Science Paper No. 205

ABSTRACT

Data acquired during the 1972 Venezuelan International Meteorological and Hydrological Experiment is used to study the thermodynamic structure of the cumulus sub-cloud layer: its time dependence, and transformation by precipitation. A close relationship between lifting condensation level (LCL) and cloud base, and between LCL and the transition layer is found. Cloud "roots" in the sub-cloud layer are identified, and the improved accuracy of the 1972 VIZ-NWS radiosonde is confirmed. Different averaging techniques are used to show the diurnal dependence of the sub-cloud layer structure. A deep slightly superadiabatic layer is found. The validity of determining surface fluxes from bulk aerodynamic formulae using the difference between surface and sub-cloud layer mean quantities is questioned. The transformation of the sub-cloud layer by precipitation is presented.

ACKNOWLEDGEMENTS

The author wishes to express his most sincere gratitude to Dr. Alan K. Betts for proposing and directing this research and giving countless hours of guidance and encouragement. Additional appreciation is extended to Ms. Linda Dugan, Ms. Polly Martin, Ms. Susan Joseph and Mr. Rick Miller who offered invaluable assistance in the manuscript typing and drafting and computer programming.

The author is grateful to the United States Air Force for the school assignment which provided the opportunity for this research to be done.

This research was partially supported by the Atmospheric Sciences Section of the National Science Foundation under Grant GA-33182. The VIMHEX II field experiment was additionally supported by the office of Naval Research under Contract NOO 014-68A-0493-002, the Facilities Laboratory of the National Center for Atmospheric Research, and the Meteorological Service of the Venezuela Air Force.

This report comprises the thesis submitted in partial fulfillment of the requirements for an M.S. degree at Colorado State University.

TITLE:

THE THERMODYNAMIC STRUCTURE OF THE

CUMULUS SUB-CLOUD LAYER

TABLE OF CONTENTS

Table of Contents - Continued

LIST OF TABLES

LIST OF FIGURES

LIST OF FIGURES - Continued

LIST OF FIGURES - Continued

LIST OF SYMBOLS

T	temperature
T_D	dewpoint temperature
T_W	wet-bulb temperature
θ	potential temperature
θ_e	equivalent potential temperature
θ_{es}	saturation equivalent potential temperature
θ_w	wet-bulb potential temperature
P	pressure
P^*	scaled pressure
e	water vapor pressure
e_s	saturation water vapor pressure
r	water vapor mixing ratio
r_s	saturation water vapor mixing ratio
RH	relative humidity
LCL	lifting condensation level
ρ	air density
z	geometric height
Q	energy
V	volume
F	flux
w	vertical wind component
(e)	environmental property
(p)	parcel property
(P)	pressure profile
$\sim$	horizontal average

$\overline{\quad}$	vertical average
$'$	deviation from mean
C_p	specific heat of dry air
R	dry gas constant
L_v	latent heat of vaporization
g	gravitational constant
ε	ratio of mean molecular weight of water vapor to that of dry air

1. INTRODUCTION

1.1 General Background

An area of meteorology where much still needs to be learned is that dealing with convective transports in the troposphere. Little is known about the contribution of convective transports to global processes and, conversely, the control exerted by large scale processes on fields of convection remains obscured.

In the literature concerning atmospheric convection, one finds a multitude of papers describing the thermal and moisture stratification of the atmosphere and the related energy fluxes that occur during convection. Consider, for example, the following description of thermal eddy size:

Warner and Telford (1967) conclude from an observational study that thermal size is about 200-300 meters and that it remains unchanged above a height of 100 meters. These results are compared favorably with aircraft and surface observations.

Vul'fson (1961) suggests an average cell diameter of 50-100 meters which changes little with height.

Grant (1965) found thermal size to increase from 200 meters in diameter near the surface to about 900 meters at a height of 600 meters and then to decrease up to the sub-cloud inversion.

Konrad (1970) based his description of convective cell growth in a clear atmosphere on observations taken by radar. This approach leads to a more complex picture in which cells of many different sizes are found at a given altitude. At a given level, a cell forms and increases in size while becoming progressively more disorganized.

Cell diameter is initially 100-200 meters but grows to 1500-2500 meters before dissipating.

The purpose of citing these results is simply to point out the state of confusion that has existed in some areas connected with atmospheric convection. It is likely that much of this difference in results is due to the difference in the method of observation and the lack of simultaneous measurements of other parameters (e.g., the energy fluxes, advective changes, wind shear, etc.) which may be of importance during convection.

The current interest in numerical models of the atmosphere has resulted in a demand for some means of parameterizing the effect of convection on the large scale circulation. This demand has led to the need for more highly sophisticated data than previously available, and has been reflected in the design of several experiments such as the 1969 Atlantic Trade Wind Experiment (ATEX) (Augstein, 1972), the 1969 Barbados Oceanographic and Meteorological Experiment (BOMEX) (Holland and Rasmusson, 1973), the 1969 and 1972 Venezuelan International Meteorological and Hydrological Experiments (VIMHEX I and II), and the proposed GARP Atlantic Tropical Experiment (GATE - 1974). This paper is concerned with some of the early results gained from data acquired during VIMHEX II.

1.2 VIMHEX II

Of the experiments which have already been carried out, two were conducted over the tropical ocean (ATEX and BOMEX) and two were conducted in the tropics over land (VIMHEX I and II). Systematic low humidities recorded during the early experiments (ATEX,

BOMEX, VIMHEX I) led to design modifications incorporated into the new VIZ-National Weather Service radiosonde. Because of the systematic humidity errors, a statistically derived correction has been applied to the ATEX, BOMEX, and VIMHEX I humidity data. VIMHEX II is one of the first major field experiments using the new VIZ-NWS radiosonde. The improved humidity measurements are discussed in Section 2.3.2.

VIMHEX II was conducted in north central Venezuela about 150 km south-southwest of Caracas. The radiosondes were launched from Carrizal which is located between the 9000 foot Coast Range 100 km to the north, and the 6000-8000 foot Guiana Highlands about 400 km to the southeast. The region has a tropical savanna climate.

Atmospheric soundings were the primary measurement taken during the experiment. There were 327 soundings taken which fell into three categories:

1. Routine soundings taken on a twice-daily basis.
2. Sequences of soundings taken on several days when convection was suppressed. These provide information about the evolution of a non-precipitating convective layer.
3. Special soundings which were made, whenever possible, before, during and after each convective precipitation event.

Additional information about the state of the atmosphere during sounding was recorded in the form of written and photographic surface observations.

The extent and intensity of convection was obtained through radar (modified M 33 - 10 cm) coverage of the area and from

precipitation measurements from a 43-gauge (21 recording gauge) network. The radar observations were recorded on photographs.

Measurements of net surface radiation were made on 57 of the 108 days that the experiment was in progress. The amount of heat conducted into the soil was measured on seven days during the experiment (see Section 2.8).

1.3 Objectives and Content of This Paper

The primary objective of this paper is the investigation of the lower portion of the convective boundary layer, i.e. the dry convective layer. The characteristic features of the heat and mositure stratification observed during dry convection will be identified and the time dependence of each feature will be described. Momentum will not be considered.

VIMHEX II has provided a large amount of coordinated data taken specifically for the study of atmospheric convection. The purpose here is to further the understanding of dry convective processes through the use of the VIMHEX II data.

The processing of the data will be the subject of Section 2. Which thermodynamic variables were computed and the reasons why they were chosen will be discussed as will be the accuracy of the data. It will be shown that the new VIZ-NWS radiosonde is accurate to about 2% of the true humidity value (except near saturation) and that the thermal lag of the hygristor is about 10 seconds. The system used to categorize each day of the experiment according to convection intensity will be described

and the method of determining an upper boundary for the dry convective layer that was used will be discussed in detail.

Pressure scaling and several different averaging techniques were employed in various parts of the study. The methods and reasons for them will also be given in Section 2.

Section 3 will deal with the non-precipitating convective layer. Structural features will be investigated first and then the time dependence of the structure. A slight superadiabatic region is observed to extend from near the surface up to about 920 mb. Some of the implications regarding the computation of heat and moisture fluxes upward from the surface will be discussed.

In Section 4, the effect of precipitation on the heat and moisture structure of the dry convective layer will be briefly examined.

2. PROCESSING OF THE DATA

2.1 Computed Variables and Interpolation

Initially, the sounding data was extracted from the strip charts of each ascent at time (one minute) intervals. This is equivalent to 20-25 mb. vertical resolution. The pressure, temperature and relative humidity were then used to compute mixing ratio, potential temperature, equivalent potential temperature and saturation equivalent potential temperature at each minute level (Appendix A). These data were then interpolated to 25 mb. levels from 975-150 mb.

This resolution is considered sufficient for the study of most of the features of atmospheric stratification. However, inspection of this data indicated that a finer resolution would be needed for the study of some of the features of the sub-cloud layer, particularly in the surface superadiabatic region.

Temperature and humidity are measured every 8-12 mb. of ascent (every "contact" level, controlled by a baroswitch). From the entire sample of 327 soundings, 138 were selected which had been taken either on days when it did not rain or prior to precipitation at Carrizal. The optimum vertical resolution of about 10 mb. was achieved by extracting the temperature and humidity measurements for the first 40 contact levels (up to about 680 mb.).

2.2 Derived Thermodynamic Variables

There is a wide choice of thermodynamic variables which can be computed from the basic set of pressure, temperature and humidity data and something should be said about the choice of variables used in this study.

The vertical distribution of temperature, T(P), as measured by radiosonde, uniquely determines the environmental vertical profiles of potential temperature (θ), saturation mixing ratio (r_s), saturation equivalent potential temperature (θ_{es}).

The combined vertical distribution of temperature, T(P), and relative humidity, RH(P), determines the environmental vertical profiles of mixing ratio (r), dewpoint (T_D), wet-bulb temperature (T_W), wet-bulb potential temperature (θ_w), lifting condensation level (LCL), and equivalent potential temperature (θ_e).

The standard presentation of radiosonde data consists of a vertical temperature profile, T(P), and a vertical mixing ratio profile, r(P), both plotted on a thermodynamic diagram such as the Skew T-log P or Tephigram. The heavy, solid lines in Figure 2.1a are the average, vertical temperature and mixing ratio profiles for all soundings taken during VIMHEX II plotted on a tephigram which has θ as ordinate and T as abscissa.

The dashed line represents the path of a parcel of dry, surface air which rises without mixing, dry adiabatically (i.e. along a constant θ-line) to the lifting condensation level where condensation begins. Above the LCL the parcel continues its unmixed

ascent moist adiabatically (i.e. along a constant θ_{es}-line). Note that the parcel conserves θ only for that portion of the ascent below its LCL, while θ_{es} is conserved throughout the entire ascent.

Since parcels of air do mix during ascent, the dashed line on Figure 2.1a represents an idealization of true parcel motion. The dotted line incorporates the effect of the entrainment of environmental air (the properties of which are given by the dark, solid lines) into the parcel. This tends to reduce the buoyancy of the parcel.

If the parcel approach is used to study convection, the important variables are those which uniquely identify the parcel throughout its ascent. If radiative effects are small, an unsaturated parcel conserves its potential temperature. Furthermore, if an unsaturated parcel mixes with a parcel of environmental air at the same pressure, the total potential heat of the parcels is exactly conserved (i.e. the extensive quantity $\int \rho c_p \theta dV$). If dry convection or the sub-cloud layer is the subject of investigation, the potential temperature is therefore a convenient thermodynamic variable.

In the more general case, where condensation occurs, the parcel conserves its equivalent potential temperature throughout its ascent and the extensive quantity $\int \rho c_p \theta_e dV$ is conserved (almost exactly) during isobaric mixing.

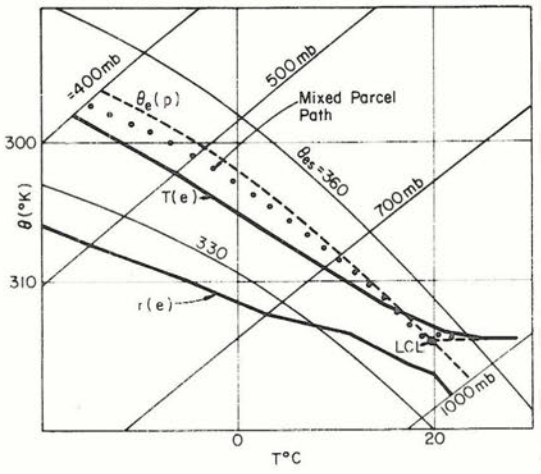

Figure 2.1a:

Standard plot of temperature T(P) and mixing ratio r(P), T_D(P) on a tephigram. Dashed line shows the path of a parcel of surface air which ascends without mixing. The dotted line is a qualitative representation of the effect of mixing. Data shown is the average of all soundings (surface to 400 mb.) taken during VIMHEX II.

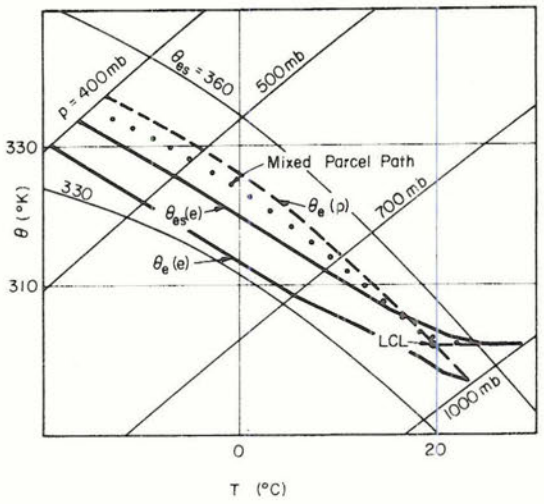

Figure 2.1b:

Same as 2.1a except vertical profile of θ_e(e) plotted instead of r(e). Note that a parcel which does not mix with the environment conserves its surface value of θ_e throughout the ascent.

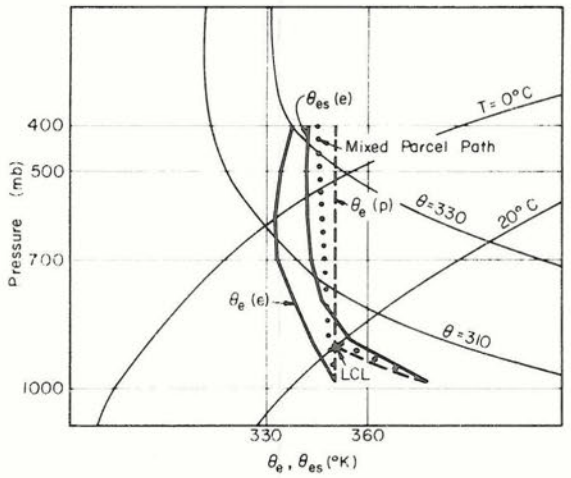

Figure 2.1c

The data is identical to that shown on 2.1b but has been plotted against P, θ_e coordinates rather that the θ,T coordinates used in 2.1a and 2.1b.

Figure 2.1b is identical to 2.1a except that the environmental vertical mixing ratio profile has been replaced by the vertical profile of equivalent potential temperature, $\theta_e(P)$, and the temperature profile has been replaced by the θ_{es}- profile which is identical.

The advantages are apparent. The parcel paths are connected to both environmental surface values and the effect of mixing is more easily visualized since both the θ_e- profile of the environment, $\theta_e(e)$, and that of the parcel, $\theta_e(p)$, are shown.

Figure 2.1c shows the final modification to the standard presentation of radiosonde data. Pressure has replaced potential temperature as ordinate, and equivalent potential temperature and saturation equivalent potential temperature have replaced temperature as abscissa. The unmixed parcel path now appears as a vertical straight line. This plot is used in Section 4.

In Section 3, the dry convective layer structure is discussed using (θ, p), (r, p) and (θ_e, p) plots.

2.3 Data Accuracy

2.3.1 Overall Accuracy of the Measurements

a) Radiosonde: The accuracy of the surface and radiosonde data (Compendium of Meteorology, 1951) used in this study is considered to be as follows:

Pressure:	±1 mb. at 1000 mb.
	±3 mb. at 500 mb.
	±1.5 mb. at 100 mb.
Temperature:	±0.2° C
Relative humidity:	±2.5%

The accuracy of radiosonde humidity measurements is discussed in Section 2.3.2.

b) Radiation: The net radiometer used during VIMHEX II has an instrumental accuracy of 4% based on a calibration precision of 2.50 ± 0.1 millivolts langley^{-1}. The average hourly radiation values were obtained using a planimeter to integrate the area under the radiation trace for each hour. The precision of this integration is about ±.05 millivolts hour^{-1}. Between 0900 LST and 1600 LST, these average net radiation values are generally greater than 5.0 mv hr^{-1}. The overall accuracy of the radiation measurements is thus 5%.

c) Precipitation: The precipitation data are used only qualitatively for this thesis. The difficulty in determining the accuracy of these measurements in terms of gauge density and location is therefore avoided. An accuracy of about 20% is considered both probable and tolerable.

d) Ground Heat Conduction: The computation of ground heat conduction is discussed in Section 3.3. It is based on measurements of soil heat content which have an estimated accuracy of 10% of the total heat content of a 70 cm. thick column of soil.

2.3.2 Radiosonde Humidity Measurements

In recent years, several questions have been raised concerning the validity of daytime radiosonde humidity measurements. Systematically low readings were recorded during the daytime ascents (Morrissey, J.F. and Brousaides, F.J., 1970; Ostapoff, F., Shinners, W.W., and Augstein, E., 1970).

The primary causes were determined to be improper shielding of the hygristor from solar radiation and possible internal heating of the hygristor by other components of the radiosonde. Another cause, about which little has been said, is the thermal lag of hygristor as the instrument passes through regions of strong vertical temperature gradient. The response of the carbon hygristor to humidity changes at 25^{o} C is less than one second (Teweles, 1970).

The modifications incorporated into the design of the VIZ-NWS radiosonde have apparently overcome the problems of shielding and internal heating (Friedman, 1972; Riehl and Betts, 1972).

One of the results obtained in Section 2.5.3 is a method of locating in the sub-cloud, air with cloudbase properties. This result will now be used to investigate the significance of the thermal lag of the radiosonde hygristor.

The set of VIMHEX II soundings which were timed as they disappeared through cloudbase, were used to determine the temperature and pressure of cloudbase from the corresponding time on the stripchart, from which the saturation mixing ratio can be obtained. It is known that the hygristor responds poorly at humidities higher than 95% (near cloudbase, see Table 2.1), so the question is whether or not air can be found anywhere below the cloud which has a mixing ratio sufficiently high that it would become saturated at the temperature and pressure of cloudbase.

The average T, r, θ, θ_e, θ_{es} and LCL at each 10 mb. level for six of these soundings which had an observed cloudbase between 910-920 mb. are listed in Table 2.1.

The average cloudbase was 915.5 mb. where the average temperature was 20.1° C requiring a saturation mixing ratio of 16.4 gm kg^{-1}. The lowest computed LCL is 913 mb. for air at 940 mb. This air at 940 mb. has a mixing ratio of 16.1 gm kg^{-1} which is 0.3 gm kg^{-1} (1.8%) below the probable value (16.4 gm kg^{-1}). Similar results are obtained for individual soundings that went into cloud.

It seems reasonable to conclude from these results that tropical daytime VIZ-NWS radiosonde humidity measurements are accurate to about 2% of the true humidity value (except near saturation, see Table 2.1).

If it is assumed that the mixing ratio at 940 mb is, in fact, 16.4 gm kg^{-1} and that the temperature (22.2° C) is accurate, then it is possible to estimate the thermal lag of the hygristor.

With these assumptions, the saturation mixing ratio at 940 mb. is 18.2 gm kg^{-1}. The correct relative humidity ($RH = r/r_s$) is 90.2% but the hygristor is measuring only 88.5%. If the hygristor is slightly warmer than the environment, then the saturation mixing ratio near the hygristor will also be higher. In fact, a relative humidity of 88.5% occurs with r = 16.4 gm kg^{-1} and r_s = 18.5 gm kg^{-1}. The saturation mixing ratio, r_s, equals 18.5 gm kg^{-1} (e_s = 27.21 mb.) at 22.5° C,

Table 2.1: Averaged data for selected soundings which entered cloud.

Averaged according to timed cloudbase 910-920. (Average 915.5 mb.)

Averaged for the following soundings -

Ascents # 49 51 112 172 198 254

Average Time = 1017 L.S.T. Average LCL = 909.0 mb.

PRESS (MB)	HEIGHT METERS	TEMP. DEG.C	MIX G/KG	TH DEG.K	TH-E DEG.K	TH-ES DEG.K	LCL MB.	NO.
994.	186.	28.3	16.6	302.0	350.6	376.0	902.	6.
980.	309.	25.6	15.6	300.6	346.0	363.8	908.	6.
970.	399.	24.7	15.6	300.6	346.1	361.0	909.	6.
960.	491.	23.9	15.6	300.6	346.1	358.5	909.	6.
950.	582.	23.1	15.6	300.7	346.3	356.3	907.	6.
940.	675.	22.2	16.1	300.6	347.4	353.8	913.	6.
930.	768.	21.3	16.0	300.7	347.4	351.5	912.	6.
920.	862.	20.4	15.3	300.7	345.4	349.2	903.	6.
910.	957.	19.7	14.5	300.9	343.2	348.0	888.	6.
900.	1052.	19.2	14.1	301.3	342.4	347.4	877.	6.
890.	1149.	18.7	13.8	301.8	342.2	347.3	867.	6.
880.	1246.	18.5	13.7	302.5	342.8	347.7	857.	6.
870.	1344.	17.9	13.2	302.9	341.8	347.2	845.	6.
860.	1443.	17.3	12.4	303.3	340.0	346.3	829.	6.
850.	1543.	16.4	11.6	303.4	337.7	344.7	815.	6.
840.	1644.	15.8	11.2	303.8	336.8	344.2	803.	6.
830.	1746.	15.6	10.9	304.6	336.9	344.9	790.	6.
820.	1849.	15.1	10.7	305.1	336.9	344.6	781.	6.
810.	1954.	14.6	10.4	305.7	336.7	344.6	769.	6.
800.	2059.	14.2	10.2	306.3	336.9	344.7	760.	6.
790.	2165.	13.5	9.4	306.7	334.8	344.0	742.	6.
780.	2273.	12.9	8.8	307.1	333.8	343.5	728.	6.
770.	2381.	12.7	8.4	308.1	333.6	344.8	709.	6.
760.	2491.	12.6	8.4	309.1	334.5	345.9	699.	6.
750.	2602.	12.0	8.1	309.6	334.4	345.6	579.	6.
740.	2715.	11.3	7.9	310.1	334.4	344.9	457.	6.
730.	2829.	10.8	7.3	310.7	333.3	345.0	336.	6.
720.	2944.	10.3	7.2	311.4	333.5	345.0	225.	6.
710.	3060.	9.7	6.6	312.0	332.5	344.9	222.	6.
700.	3178.	8.9	6.1	312.4	331.3	344.1	111.	6.
690.	3297.	8.2	5.9	312.9	331.1	343.5	111.	6.
680.	3418.	7.5	6.3	313.5	333.1	343.4	132.	5.
670.	3546.	6.5	5.8	313.6	331.7	341.8	0.	3.
660.	3669.	6.0	5.1	314.4	330.4	342.1	0.	3.
650.	3794.	5.3	4.4	315.1	328.9	342.1	0.	3.

GM. of Precipitable Water = 3.56
Thickness 980 to ≤700 = 2869.
Mean Column θ_e = 339.5

0.3^{o} C above the ambient temperature. This temperature would be found at about 943 mb. If the balloon rises at a rate of 20 mb. min^{-1}, the thermal lag of the hygristor is about 9 sec.

2.4 Categorization of Convection

It is convenient, in an observational study of convection, to categorize the data in terms of the intensity of the convection. The average daily precipitation measurements from 23 selected gauges were used to objectively categorize each day of the experiment as a "dry" or a "wet" day. On "dry" days, the convection was suppressed while on "wet" days, the convection was deep.

Four categories were defined so that Categories I and IV consisted of the extremely dry and extremely wet days, respectively. The division between Categories II and III was chosen arbitrarily. The criteria are listed in Table 2.2 along with the number of days and soundings in each category.

Table 2.2: Categories of convection.

Category	Average Area Precipitation (mm)	Number of Days	Number of Soundings
I	< 0.1	23	44
II	0.1-2.0	36	98
III	2.0-5.0	19	72
IV	> 5.0	21	91

(Note: 22 soundings were taken prior to precipitation measurements.)

2.5 Determination of the Top of the Dry Convective Layer

2.5.1 General Approach

Considerable effort was spent developing a means of determining the top of the non-precipitating convective layer so that diurnal changes in the depth of the layer could be studied. A number of VIMHEX II soundings were observed to enter cloud. A cloudbase height was determined for several of these ascents by measuring the time at which the balloon entered cloudbase, and finding the pressure corresponding to this time from the rawinsonde strip chart. This observed cloudbase was related to LCL values in and the structure of the sub-cloud layer for the same soundings, and finally, to the dry convective structure between the clouds.

2.5.2 Data Used

The soundings used for the remainder of this section were taken either: (1) on days when there was little or no precipitation, or (2) prior to precipitation on days when it rained at Carrizal. The vertical resolution of the soundings is 10 mb. (see Section 2.1). There were 138 soundings in this group, of which 26 were observed to enter cloud. The distribution with respect to the previously defined categories of convection is shown in Table 2.3.

Table 2.3: Distribution of data with respect to category of convection.

Category of Convection	# of Soundings Outside Cloud	# of Soundings Into Cloud
I	35	4
II	45	11
III	18	6
IV	14	5
Total	112	26

2.5.3 LCL Computation

A timed cloudbase was available for 22 of the 26 soundings that were observed to enter cloud. The LCL was computed (see Appendix A) at each 10 mb. level for each of these 22 soundings. If a balloon enters cloud it must also, at some level below the cloudbase, enter air which is going into cloud and has cloudbase properties (i.e. an LCL which corresponds roughly to the height of the cloudbase). This was the case in 14 of the 22 soundings. It was assumed that the remaining eight had either entered cloud somewhere above cloudbase or passed through a very shallow cloud and therefore they were not used.

The simplest way to compute an LCL rests on the assumption that surface air rises vertically into cloud. The temperature and mixing ratio measured at the surface can then be used to compute an LCL and thus an approximate height of cloudbase. This procedure does not account for mixing of the surface air with the cooler, drier air aloft. The effect of mixing may be incorporated

by computing the LCL at some level above the surface (e.g. 950 mb.) or by using an average of the LCL's computed at several levels.

Examination of the 14 VIMHEX II soundings shows that if the properties of surface air are used in the LCL determination of the height of cloudbase, the predicted cloudbase is often 20-30 mb. too high (i.e. at a lower pressure). Using the 950 mb. air shows no significant improvement. In fact, there is no one level which gives consistently reliable results.

The problem then is to determine which levels should be used to determine an average LCL. Examination of the LCL profiles of the soundings which went into cloud reveals the following features which are common to both individual soundings and to averages of several of the soundings (see Figure 2.2):

a) A surface LCL which is generally 10-20 mb. too high and occasionally as much as 30 mb. too high.

b) High LCL's at several levels near the surface.

c) Either a gradual or discontinuous shift to lower LCL's which are very near the observed cloudbase. In 13 of the soundings, the lowest LCL in this region was within 5 mb. of cloudbase. The exception was a minimum LCL that was 10 mb. above cloudbase.

d) The levels above the minimum value show high LCL's which are due to the inability of the radiosonde hygristor to respond near saturation.

If the assumption that surface air rises vertically into cloudbase is modified, then a reasonable explanation of these features is possible. The basis of the explanation is the fact

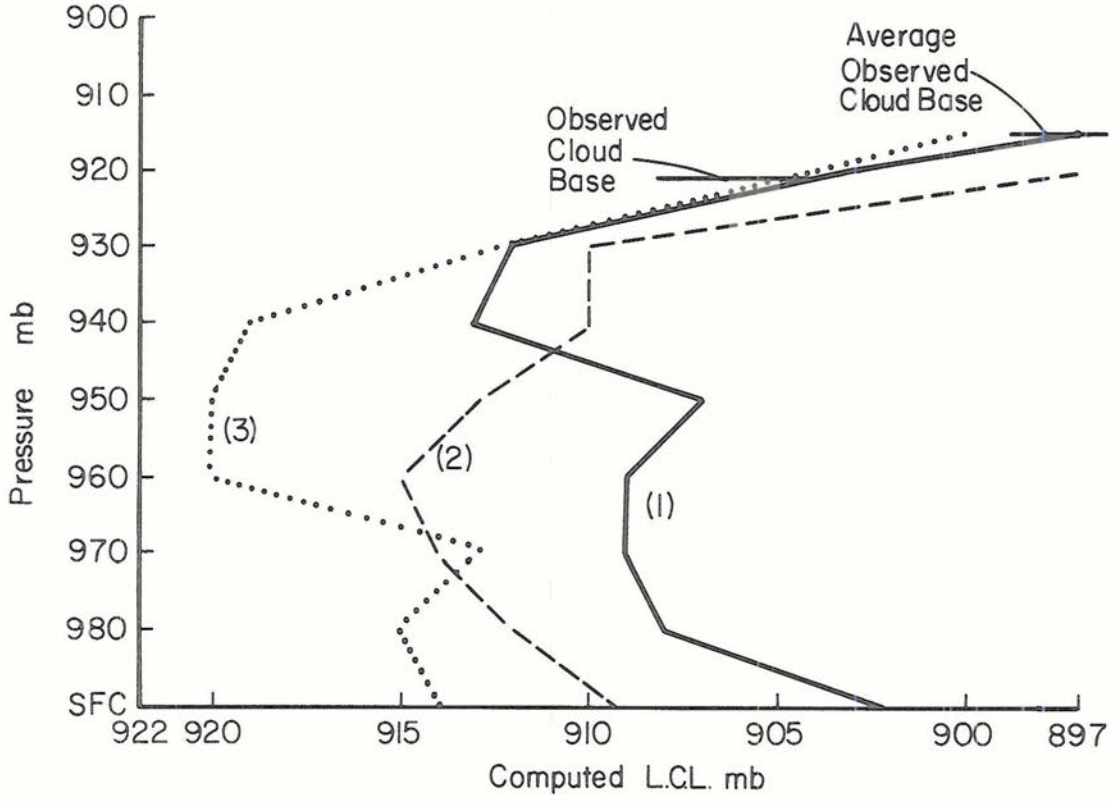

Figure 2.2: Lifting condensation level of air.

At each 10 mb level of:

(1) average of soundings which passed through an observed cloudbase between 910-920 mb (solid line)

(2) average of soundings with a L.C.L. between 910-920 mb which did not enter cloud (dashed line)

(3) VIMHEX II ascent #63 which passed through an observed cloudbase at 921 mb (dotted line)

that cumulus clouds are most often observed moving in a wind-shear field. It is reasonable to assume that the currents of air entering cloud as well as the motions induced in the environment around the cloud are tilted away from the vertical by the vertical wind shear.

This effect is illustrated schematically in Figure 2.3. The air near the surface at point A is subsiding and is therefore relatively warm and dry and would have a high LCL. The air which is entering the cloud is originally located at the surface at some point to the left of A. This air is found at about 960 mb. above point A.

A radiosonde launched at point A would measure temperatures and humidities that would lead to a vertical LCL profile very similar to that described above. The mean LCL computed from the average of all soundings with an observed cloudbase between 910-920 mb. has been given in Table 2.1 as an example. The wind indicated in Figure 2.3 is the mean for this data sample.

An iterative scheme was devised, based on these considerations, which first averaged the LCL's computed at each 10 mb. level from 980 mb. to 930 mb. This was used as a first "guess." The first iteration averaged the LCL's at each 10 mb. level from 980 mb. to 30 or 40 mb. below the "first guess" depending on the height of the "first guess." The LCL's at and 30 to 40 mb. below cloudbase are erroneously high due to limitations of the radiosonde hygristor and were, therefore, not used in the average. A second iteration was performed using the result of the first iteration

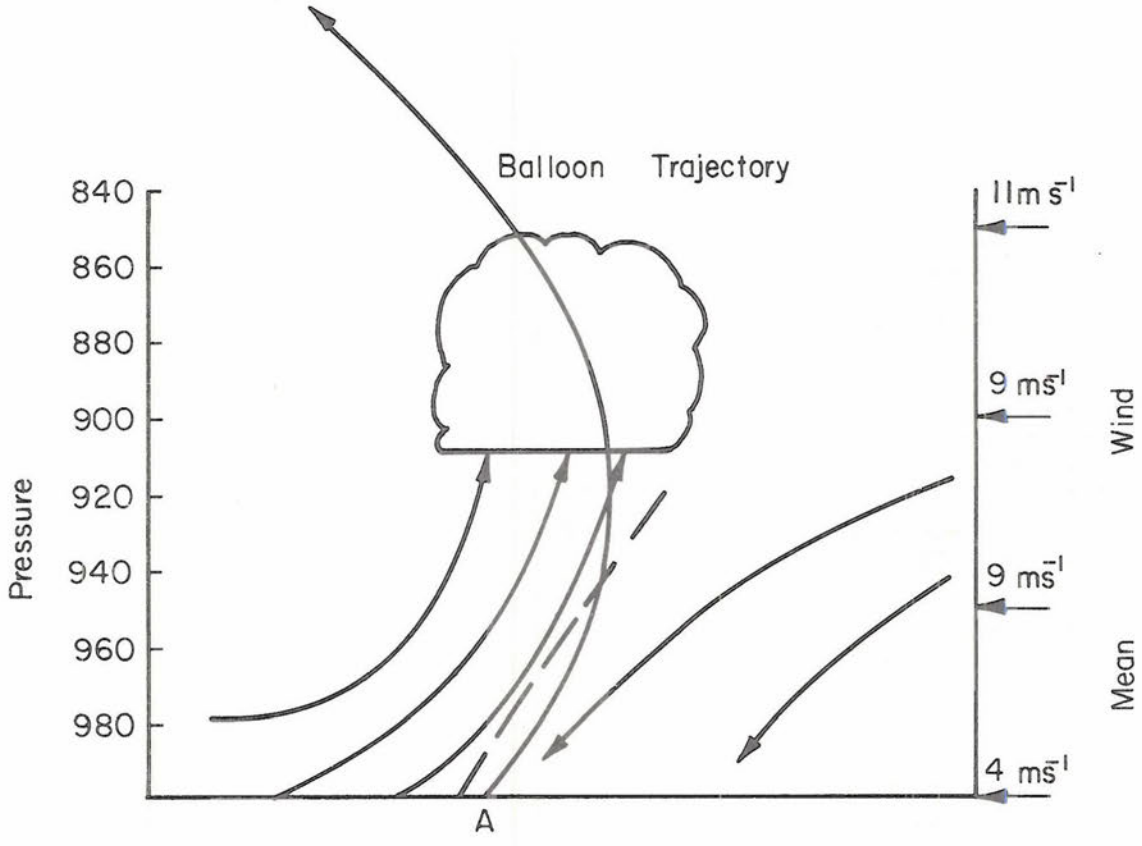

Figure 2.3: Suggested circulation relative to cloud.

as a "second guess." The mean LCL which was then obtained was found to be reasonably close to the observed cloudbase. The observed cloudbase and computed LCL are compared in Table 2.4.

Table 2.4: Height difference between mean LCL and cloudbase.

Radiosonde #	49	51	63	79	85	109	112	114	115	141	156	172	198	254
Observed Cloudbase (mb)	915	912	921	909	906	886	914	868	850	924	924	917	919	916
Mean LCL (mb)	914	907	919	907	898	882	909	866	844	911	917	910	904	909
Difference (mb)	+1	+5	+2	+2	+8	+4	+5	+2	+6	+13	+7	+7	+15	+7
Average Difference: +6 mb.														
Extremum LCL	917	908	920	910	901	888	914	871	847	922	924	914	909	921
Difference (mb)	+2	-4	-1	+1	-5	+2	0	+3	-3	-2	0	-3	-10	+5
Average Difference: -1 mb.														

The LCL extremum values in Table 2.4 are the lowest LCL's in the subcloud layer (see also Table 2.1 and Figure 2.2). This extremum LCL corresponds most closely to the observed cloudbase. Averaging the LCL's computed at six levels (980-930 mb.) yields a mean value which is slightly but consistently high. The use of the lowest computed LCL in each profile, rather than a mean value, may afford some improvement in the correspondence between the computed LCL and the true cloudbase. This was not, however, done in this study, the conclusion is retrospective.

2.5.4 The Relation of the Computed LCL to Sub-cloud Structure

If the computed LCL is to be used as an upper bound of the dry convective layer, it is necessary to show that it is, in fact, located at the top of that layer. The feature of the thermal structure of the sub-cloud layer which is most visible both in individual and average θ-profiles is the mixed layer or the region where θ is nearly constant with height. The top of this layer (i.e. the level above which θ begins to increase more rapidly with height) has been estimated and is compared to the LCL in Table 2.5. The evidence is that the thermally mixed layer extends up to cloudbase. On the average, the LCL is found slightly above the top of the mixed θ layer under clouds, but the difference is not significant.

Table 2.5: Height difference between the mean LCL and the top of the θ mixed layer.

Sounding Number	Observed Cloudbase (mb)	Mean LCL (mb)	Estimated Top of θ Mixed Layer (mb)	ΔP: Top of Mixed θ Layer to Cloudbase (mb)	ΔP: LCL to Top of Mixed θ Layer (mb)
49	915	912	910	-5	+2
51	912	907	900	-12	+7
63	921	917	920	-1	-3
79	909	908	910	+1	-2
85	906	899	900	-6	-1
109	886	883	880	-6	+3
112	914	912	920	+6	-8
114	868	865	860	-8	+5
115	850	844	840	-10	+4
141	924	914	920	-4	-6
156	924	918	930	+6	-12
172	917	911	910	-7	+1
198	919	905	920	+1	-15
254	916	909	910	-6	-1
Average				-4	-2

2.5.5 The Relation of the Computed LCL to Dry Convection In Clear Regions

Thirty-two of the soundings which were not observed to enter cloud were selected on the basis of having well-defined mixed layers and transition zones. The purpose here is to justify the application of a mean LCL, determined using sub-cloud data, to regions above which there are no clouds. The soundings were averaged according to the estimated height of the base of the transition layer. The results are shown in Table 2.6.

Table 2.6: Height difference between the mean LCL and base of transition zone not below cloud.

# of Soundings in Average	Estimated Base of the Transition Layer (mb)	Average LCL (mb)	ΔP (LCL-top of Mixed Layer) (mb)
5	890	883	-7
7	900	889	-11
13	910	897	-13
5	920	912	-8
		Average	-10

The mean LCL is here located above the top of the mixed layer. For the remainder of this paper, the mean LCL will be considered to be the upper boundary of the non-precipitating convective layer below cloud and in regions where there are no clouds.

2.6 Pressure Scaling

Since the depth of the dry convective layer varies significantly from day to day as well as diurnally, averaging often results in structural features which are present on the individual soundings being blurred beyond recognition. The averaging techniques which were used to minimize this are discussed in the next section. Vertical scaling of the soundings permits an easier comparison of the structure of individual soundings and allows the averaging of large numbers of soundings without the loss of definition that would be expected due to variations in the depth of the layer.

The logical choice of a scale height is the mean LCL described in the previous section. The scaling was done simply by defining a scaled pressure:

$$P^* = \frac{P_{surface} - P(I)}{P_{surface} - P_{LCL}} \qquad (2.1)$$

where I indicates the particular data level.

It can be seen that when $P(I) = P_{surface}$, $P^* = 0.0$ and when $P(I) = P_{LCL}$, $P^* = 1.0$.

2.7 Averaging Techniques

2.7.1 Selection of Data for Averaging

Averaging, by any method, is bound to result in some smoothing of the data. The amount of smoothing depends on the amount of data selected for averaging. A large sample of data can be subdivided in many different ways and certain subdivisions will result in subtle differences in the averages that are obtained.

When radiosonde data is to be used in the study of the dry convective layer, there are two obvious ways the data might be grouped. First of all, the soundings can be arranged according to the time the balloon was released and then all the soundings within a specified time interval can be used to obtain an average for that time period. This will be called a time average.

A second method is to arrange the soundings according to the mean LCL (Section 2.5), select certain intervals of the LCL values and average the soundings that fall into each interval separately. This will be referred to as an LCL average.

A third, not so obvious, method is to select a time of day, say 1000 LST, as a reference time and consider a sounding taken within a certain interval of that time, say 0900-1100 LST as a reference sounding. This sounding can then be subtracted, variable by variable, from every other sounding taken on the same day and a difference from the reference time obtained. These differences represent the change in the atmosphere from the reference time, and may be averaged separately before being added to the average of the reference soundings. This will be called a difference average.

The next several sub-sections will be used to describe the differences between these three types of averages. The data used is the set of 112 non-precipitating convective soundings (Section 2.5.2).

2.7.2 Time averages

The convective period (0700-1900) was divided into six two-hour time periods for time averages used in this paper.

The soundings in the sample used here were all taken between 0700 and 1700 LST. There was a relatively large number of soundings in each time interval. Inspection of the five average θ-profiles revealed that most of the structural features which do appear on individual soundings were smoothed out. The mixed layer, or the layer in which θ is approximately constant with height was reasonably defined in only two of the five averages (average times: 1005 and 1144 LST).

This smoothing results from the fact that at a given hour of the day, the depth of the dry convective layer varies greatly from day to day. This variation must be included if the reason for the average is the study of the diurnal change of the mean structure but it is a serious defect if one wishes to study specific structural features.

2.7.3 LCL Averages

To eliminate the smoothing of the time averages, the soundings were sorted into fifteen (fourteen 10 mb. and one 40 mb.) intervals according to LCL. This is a grouping of the soundings in the original set in such a way as to restrict the depth variation of the layer to the size of the LCL interval. The mixed layer can be defined to within ±10 mb. on eleven of the fifteen averages. There is an inherent time dependence here since the dry convective layer is observed to deepen through the day. The changes in the LCL averages with time do not necessarily reflect changes of a mean structure with time since, by design, a significant portion of the variation which goes into the time average has been removed.

2.7.4 Difference Averages

The fluxes which occur in the dry convective layer are linked to the absorption of solar energy at the earth's surface. It is reasonable to assume that during any period of the day, there are similar daily changes in the heat and moisture stratification between the beginning and end of the period since the change in insolation will generally be the same.

The difference average requires a mean reference structure based on a large enough set of soundings to ensure that the day to day changes in structure have canceled each other out. If this is the case, then this method gives the most accurate mean daily changes which are crucial to accurate mean flux computations.

3. THE NON-PRECIPITATING CONVECTIVE LAYER

3.1 Description

The energy input into the dry convective layer and each of the features of the sub-cloud layer will now be investigated using the VIMHEX II data. The objectives will be: (1) to determine how well the model structure proposed by Betts (1973; Figure 3.1) represents the structure as observed during VIMHEX II and, (2) to determine the variability of each feature during the course of a "typical" dry convective day. It is hoped that by using this relatively large amount of high resolution data, a more precise picture of dry convection will be obtained.

Betts (1973) shows the thermal stratification of a typical (i.e. model) dry convective layer (Figure 3.1). The dry convection layer is composed of three regions, each with a distinct potential temperature lapse rate, and is capped by a "cumulus" layer where θ increases with height.

The superadiabatic layer develops diurnally as the earth's surface is heated by solar radiation. There is a net flux of sensible heat upward through this region into the mixed, or dry adiabatic, layer. This flux is the driving force which determines the thermal structure of the dry convective layer. Most of the shear turbulence in the lower atmosphere is generated in this lower layer. Ball (1960) has shown that the amount of shear turbulence generated is about one-tenth of the amount of thermal turbulence.

Thermal eddies are formed as parcels of air near the surface are heated and become buoyant. The eddies travel upward through

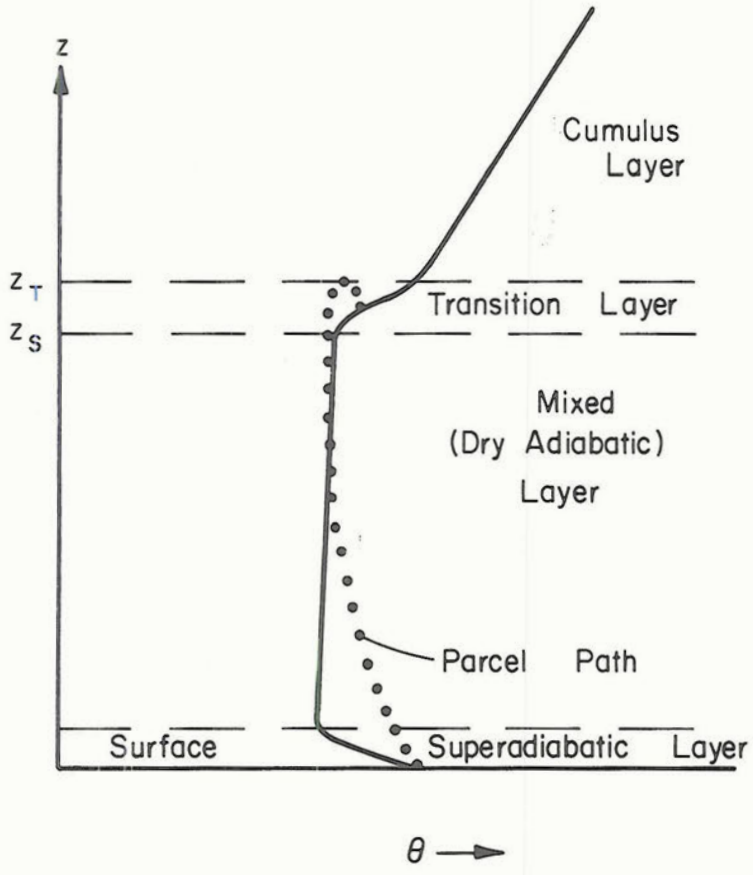

Figure 3.1: Model dry convective layer structure after Betts (1973).

the dry adiabatic layer, losing buoyancy by mixing with the cooler environmental air and through viscous dissipation. The turbulent mixing results in a constant or slightly increasing vertical θ-profile in the mixed layer.

Any buoyant kinetic energy which the parcel has when it reaches the level where its potential temperature is equal to that of the environment will cause it to overshoot the equilibrium position. During the "overshoot" mixing will cause a cooling of the environment. The transition layer marks the top of the dry convective layer. Its height is determined by the amount of "overshoot" and the resulting cooling of the environment (Betts, 1973).

3.2 Observed Structure

3.2.1 General Considerations

The variation in the depth of the dry convective layer has been previously discussed. It has been shown that in order to study average structural features of the heat and moisture stratification in the layer, the effect of this variation in averaging must be restricted. This will be accomplished by using LCL averages (Section 2.7.3), by averaging soundings which have been scaled vertically (Section 2.6), and by using a subset of soundings which have particularly good structural definition. Both the thermal (θ) and moisture (r) stratifications will be considered.

3.2.2 LCL Averages

One hundred twelve non-precipitating convective soundings (Section 2.5.2) were used to construct the LCL averages. Between

940-790 mb. a 10 mb. LCL interval was used. All the soundings with LCL's higher than 790 mb. were grouped into one 40 mb. interval, 790-750 mb. All 112 soundings had mean LCL's within this range but none fell into the 930-920 mb. interval. There were, therefore, 15 LCL averages obtained.

Nine of the average θ-profiles are plotted on Figure 3.2. Only data to the first interpolated level above the mean LCL is plotted and dotted lines are used where needed to avoid confusion. The corresponding moisture profiles are shown separately on Figure 3.3.

a) Thermal Structure (Figure 3.2): The same general features as those shown on Figure 3.1 may be seen in each of the average θ-profiles. There is a sharp decrease in θ in the layer just above the surface. Since 980 mb. is the lowest interpolated level, the averages show that a sharp decrease occurs between 980 mb. and the surface. Above 980 mb. θ is observed to be nearly constant with height up to a level 30-50 mb. below the mean LCL. Above the "constant-θ" or mixed layer the averages show a gradual increase of θ with height.

The sharp θ-decrease near the surface averages about 1.0-1.5^{o} K. The uniformity of this feature suggests a rather steady energy flux through the layer nearest the surface regardless of the depth of the dry convective layer. The exception to this is the average profile for the sounding with LCL's above 790 mb. Here the θ-decrease is only 0.4^{o} K. Since the deepest dry convective layers occur

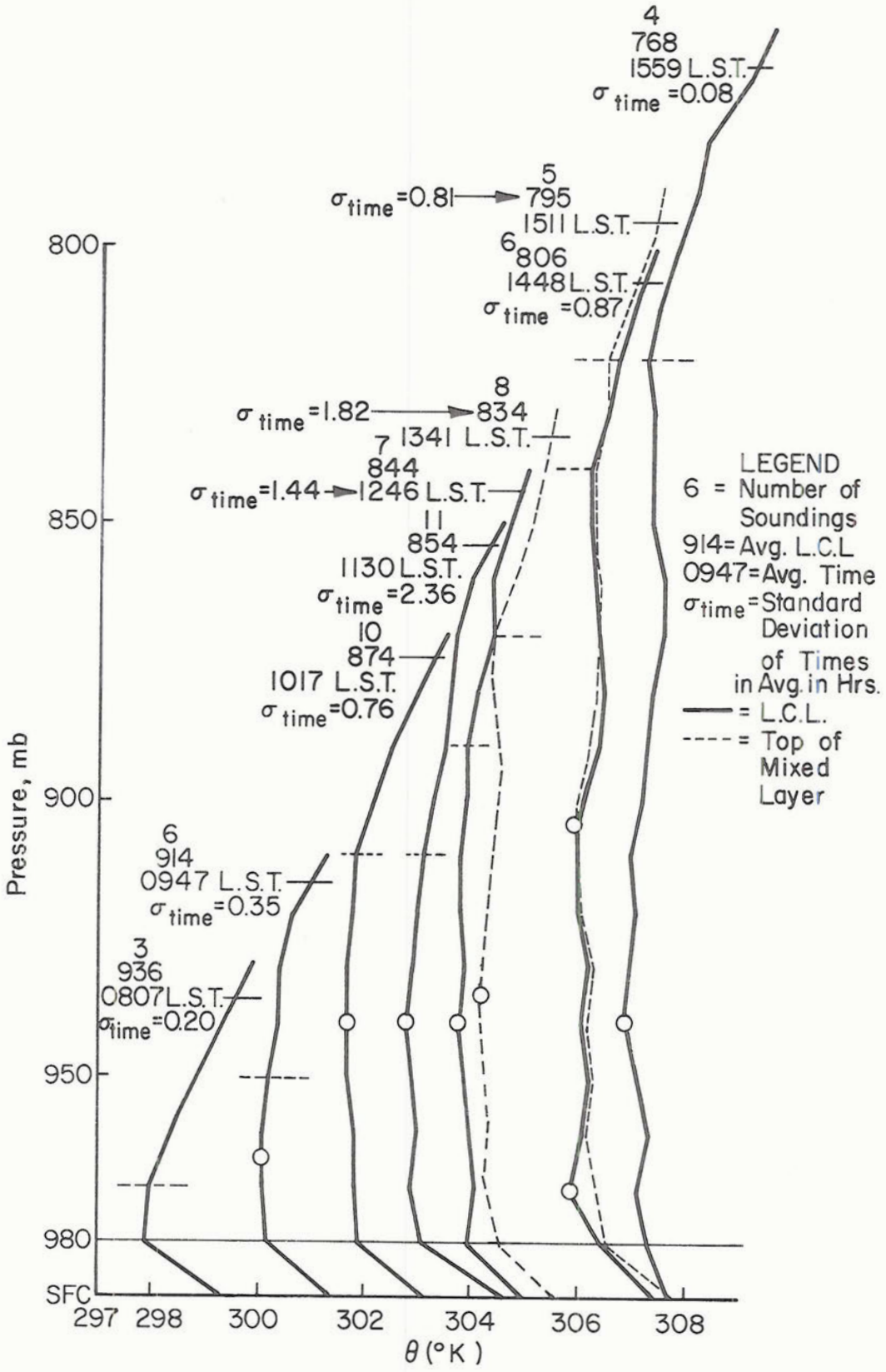

Figure 3.2: Graph of potential temperature (θ) against pressure for sets of L.C.L. averaged data.

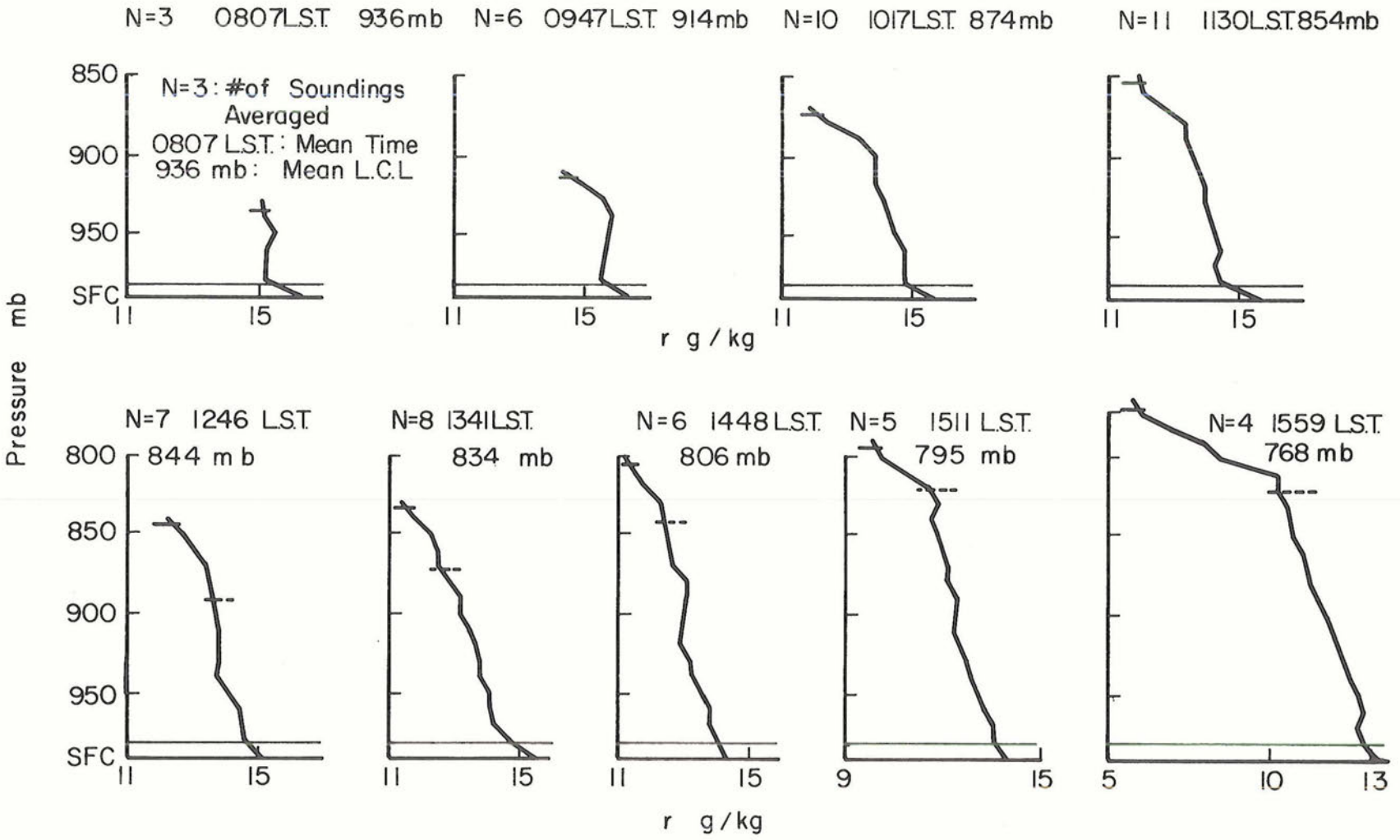

Figure 3.3: Surface to L.C.L. moisture (r) profiles for L.C.L. averaged dry convective soundings.

late in the day, this exception reflects the decrease in surface temperature that also occurs late in the day. It follows that the potential temperature of the mixed layer is about 1.0-1.5^{o} K cooler than the surface temperature.

An interesting feature observed on many of the individual soundings and in eight of the nine LCL averages introduces some ambiguity into the definition of "surface superadiabatic layer" and "mixed layer" as shown on Figure 3.1. This feature is the minimum value of θ between 980 and 900 mb. The minimum is circled on each profile shown on Figure 3.2. Since the highly unstable region is generally confined to a layer near the surface, it is more consistent to interpret this θ minimum as a feature of the mixed layer rather than as an extension of the surface superadiabatic layer.

For LCL's below 840 mb., the θ-minimum is found at or below 940 mb. and the sharp θ-decrease near the surface is confined below 980 mb. However, for higher LCL's, the position of the θ-minimum in the layer varies widely and the strong θ-decrease near the surface extends up to 970-960 mb. Possibly, as a dry convective layer deepens, the thermal structure of the layer becomes more complex.

b) Moisture Structure (Figure 3.3): There is a 0.5-1.0 gm kg^{-1} decrease in mixing ratio from the surface to 980 mb. until the LCL reaches 830 mb. For deeper layers (late in the day), this decrease is less than 0.5 gm kg^{-1}. Strong vapor fluxes from the surface are therefore implied only

while the layer is developing. The surface vapor flux is apparently less significant as the layer reaches full development.

When the dry convective layer is shallow (i.e., LCL below 900 mb.) the mixing ratio is nearly constant in the mixed layer. This might be because convection has not reached the LCL early in the day, and as yet there are no dry downdrafts from the cumulus layer. For LCL's above 900 mb., the mixing ratio is seen to decrease through the mixed layer by about 1.0-2.0 gm kg^{-1}.

The mixing ratio lapse rate changes abruptly at or near the top of the mixed layer, from about -2 gm kg^{-1} (100 mb.)$^{-1}$ to -7 gm kg^{-1} (100 mb.)$^{-1}$. The sharpness of this discontinuity is a result of the mixing of the moist convective elements at the top of their ascent and the simultaneous entrainment and mixing of dry air downward through the LCL.

3.2.3 Pressure Scaled Average

The entire set of 112 dry soundings which did not enter cloud were scaled according to the LCL and then averaged. The average mean LCL is 861 mb. and the average time 1145 LST. The θ- and r-profiles are plotted on Figure 3.4. The ordinate, P*, in Figure 3.4 is the pressure scaled to the height of the LCL (see Section 2.6).

a) Thermal Structure: The strong θ-decrease is observed to be below P* = 0.05. Between P* = 0.1 and P* = 0.5, the air has been extremely well mixed. Potential temperature increases slightly (0.1^{o} K (10 mb.)$^{-1}$) between P* = 0.5 and

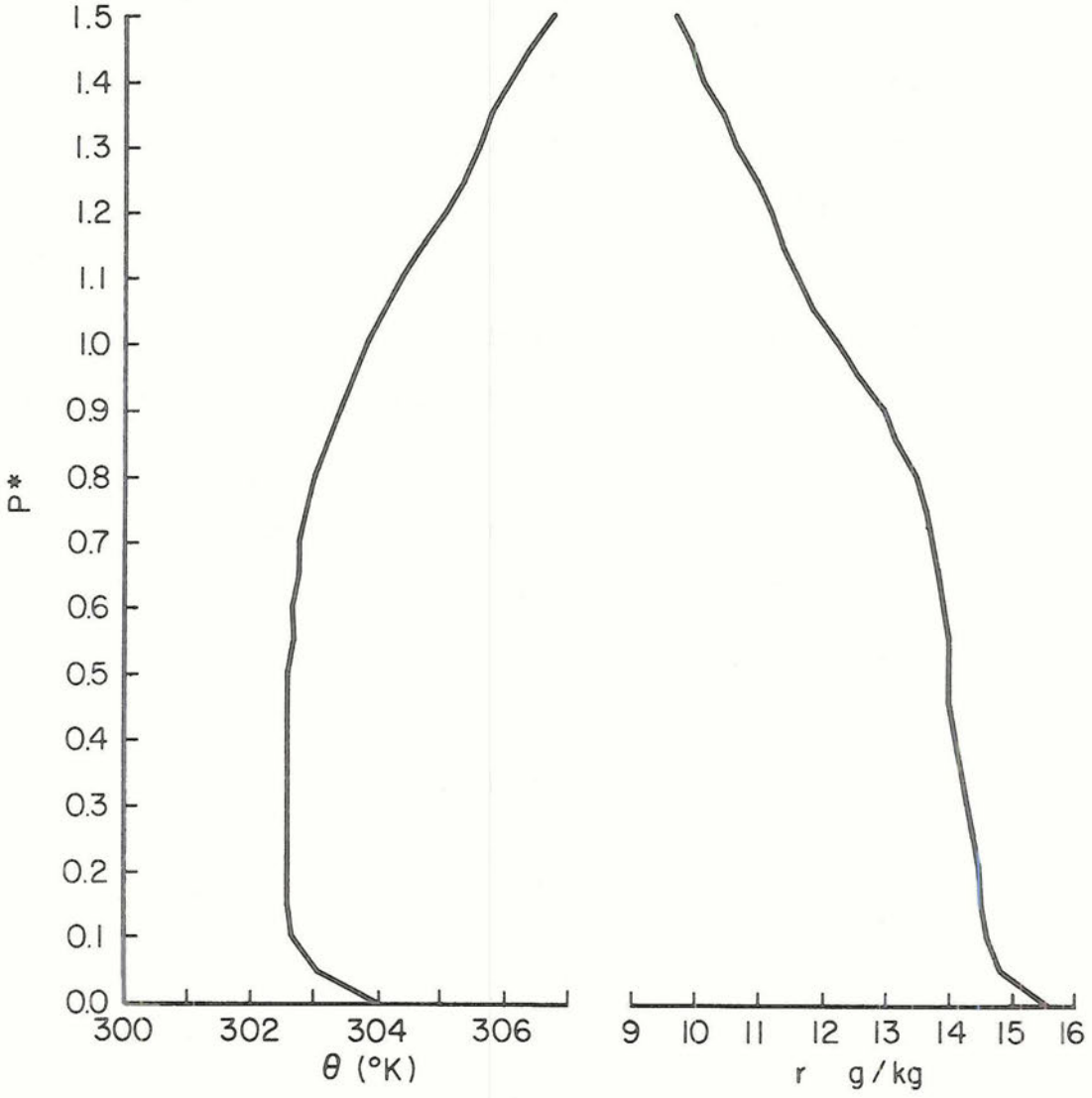

Figure 3.4: Graph of potential temperature (θ) and mixing ratio (r) for mean of 112 P-scaled dry convective soundings.

P* = 0.8 but a more marked increase (about 0.4^{o} K (10 mb.)$^{-1}$) probably indicating the mean top of the mixed layer, begins at P* = 0.8. The potential temperature at the LCL is approximately the same as the surface potential temperature.

Figure 3.4 indicates that the thermal driving force of convection is found in the lowest tenth of the layer. It is possible that the previously discussed θ-minimum has been smoothed out, especially since it does not appear to have a fixed position in the layer relative to the LCL (see Figure 3.2). The mean atmosphere is seen to be unstable or neutral in the lower half of the dry convective layer and stable above P* = 0.5.

b) Moisture Structure: The large decrease in mixing ratio is similarly confined below P* = 0.05. Above P* = 0.05, the mixing ratio decreases with height. The water vapor is apparently well mixed up to P* = 0.8 where it begins to decrease more rapidly with height. The region of sharpest moisture decrease is found approximately between P* = 0.8 and P* = 1.05.

The largest decreases in moisture occur near the surface and between P* = 0.8 and P* = 1.05. One might, therefore, expect the strongest moisture fluxes to be upward from the surface and upward through the LCL, using the downgradient transport hypothesis.

3.2.4 Average of Soundings With a Well-Defined Transition Zone

Since the transition zone at the top of the dry convective layer was not detectable on either the LCL average or pressure-

scaled average profiles, a set of 30 soundings where this feature was well defined was selected from the original sample. The 30 soundings were divided into four 10 mb. mean LCL intervals and then averaged. The 30 selected soundings comprise 71% of the original data within these LCL ranges.

The four mean θ-profiles are plotted on Figure 3.5. Each profile has been divided into layers corresponding to Figure 3.1. Since the superadiabatic and mixed layers have already been discussed, it will only be noted that on three of the four profiles, the lower portion of the mixed layer is unstable as shown earlier.

The reason for the selection of these is to examine the stable transition layer. The upper and lower boundaries of the layer were determined by extrapolating the less stable lapse rate above the LCL downward and by estimating the level below the LCL where θ begins to significantly increase with height. These boundaries are shown by the dashed lines on Figure 3.5.

The transition zone is located in the region 10 mb. below to 10 mb. above the LCL. Its average depth is 10-20 mb. The potential temperature lapse rate above the zone is $+4\text{-}5^{o}$ K/100 mb. while in the zone it averages $+8.25^{o}$ K/100 mb.

3.2.5 A Comparison of a Mean Dry Convective Layer Not Below Cloud With a Mean Sub-Cloud Layer

Some differences are to be expected between soundings through clear air and those that enter cloud. In order to determine whether or not differences in structure do exist, the mean θ- and r-profiles of all P-scaled soundings which did not enter

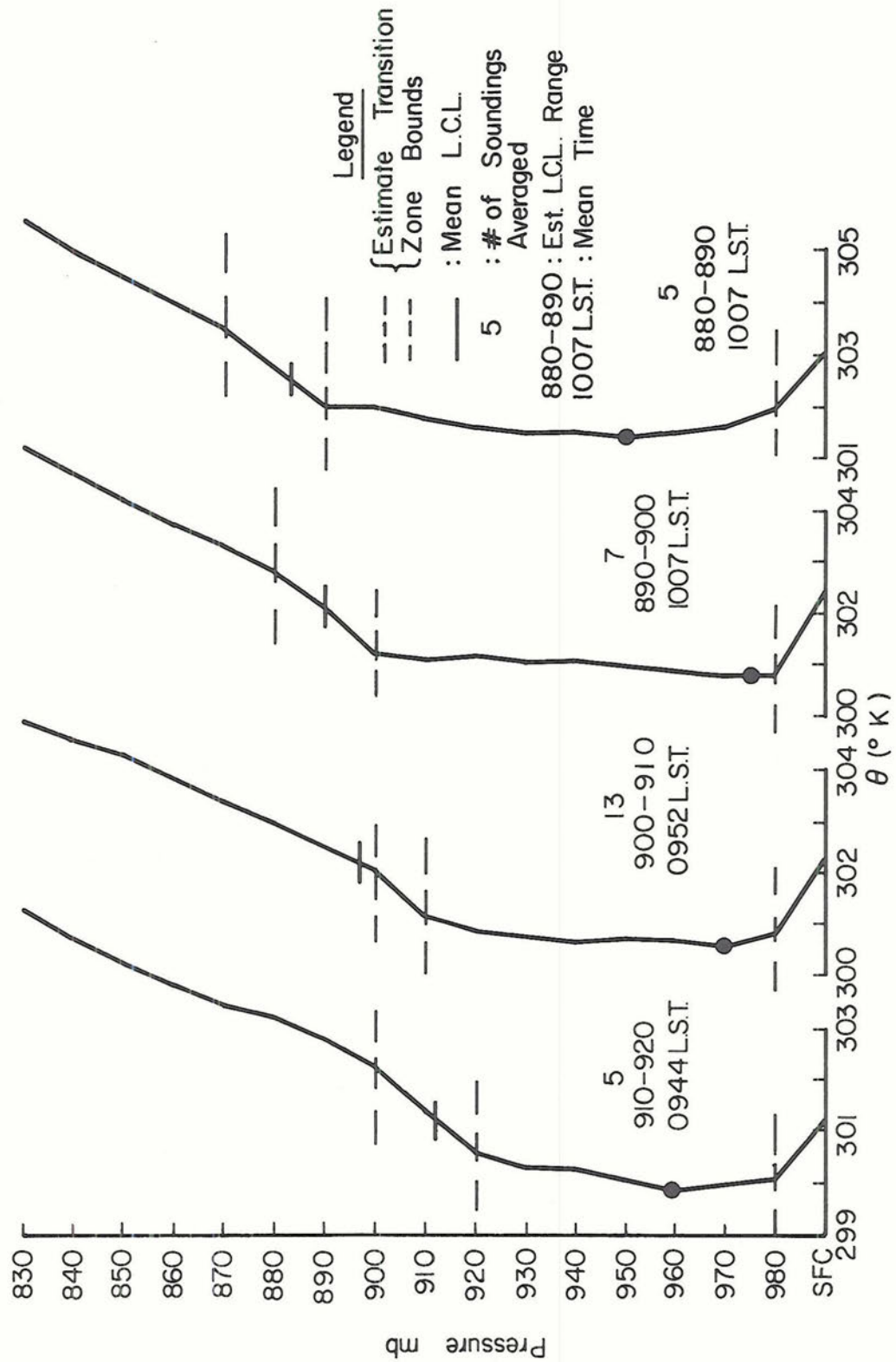

Figure 3.5: Vertical θ-profiles for selected L.C.L. averaged, dry convective soundings.

clouds were compared with the set of P-scaled soundings which did enter cloud (Figure 3.6). An additional comparison was made between a set of "into-cloud" and "outside-cloud" soundings which had cloudbase or a transition zone between 910-920 mb. (Figure 3.7), taken from Table 2.1 and Figure 3.5.

The difference in the extent of mixing in the dry convective layer can be seen in both the θ- and r-profiles plotted on Figure 3.6. The dry convective layer below cloud is thermally well-mixed between P* = 0.1 and P* = 0.95 while the moisture is nearly constant from P* = 0.05 to P* = 0.80; the fall from P* = 0.8 to P* = 1.0 is probably instrumental (see section 2.3.2). Away from clouds the dry convective layer is well mixed thermally from P* = 0.1 to P* = 0.5 and slightly stable from P* = 0.50 to P* = 0.80 where θ begins to increase significantly with height. Moisture decreases slowly with height from P* = 0.05 to P* = 0.80 away from clouds. Above P* = 0.80 it begins to decrease more rapidly.

The profiles shown on Figure 3.7 show essentially the same features. The "into-cloud" soundings are thermally well-mixed up to the LCL (909 mb.). There is a mixing ratio maximum about 30 mb. below the LCL showing the air with cloudbase properties (Figure 2.2). Away from clouds, the thermal structure is unstable to 960 mb., slightly stable between 960 mb. to 10 mb. below the LCL, and markedly stable above 920 mb. The mixing ratio away from clouds is nearly constant between 980-930 mb. above which it decreases with height.

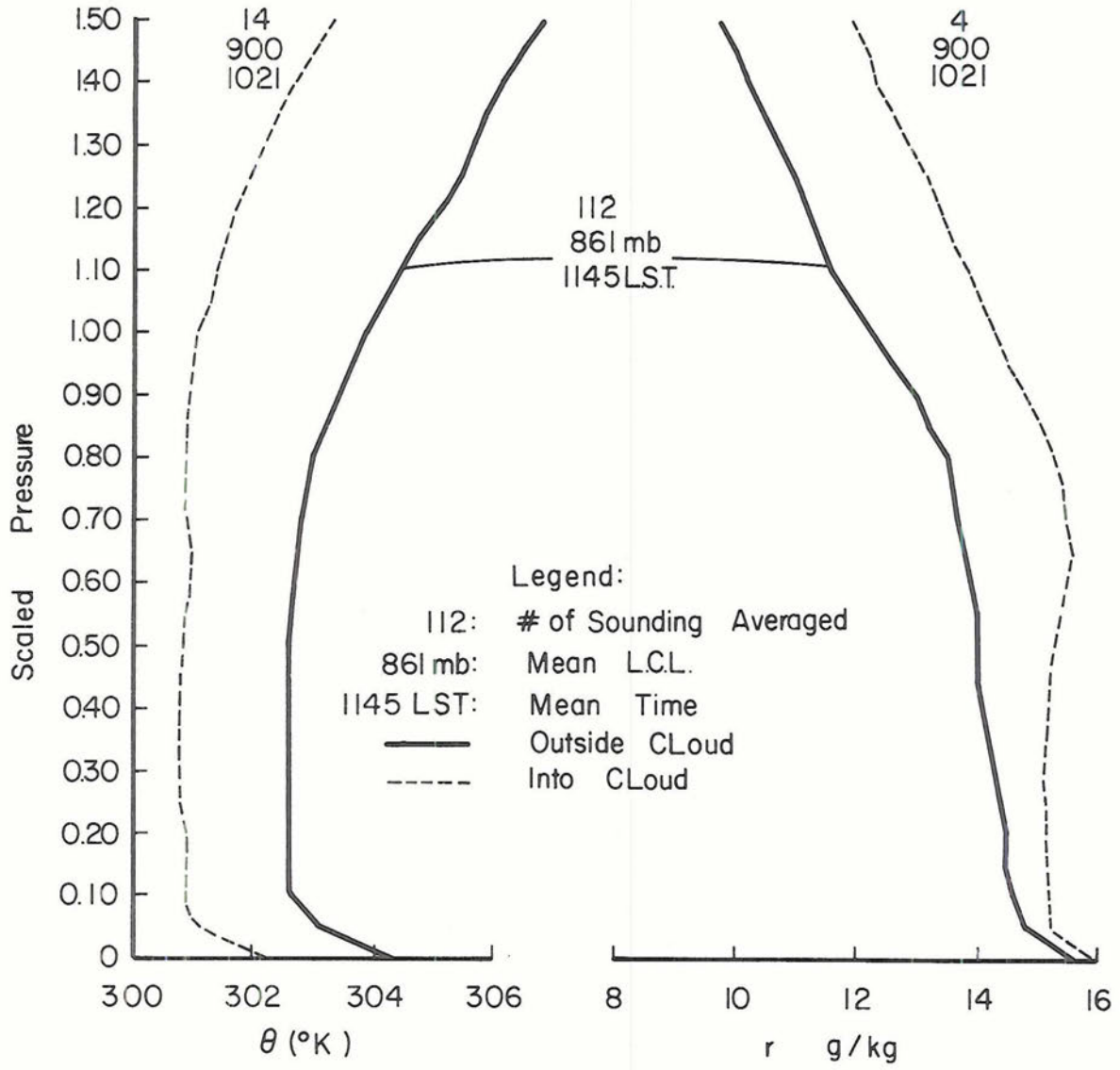

Figure 3.6: Potential temperature (θ) and mixing ratio (r) vertical profiles for mean outside-cloud (solid line) and mean selected into-cloud (dashed line) P-scaled soundings.

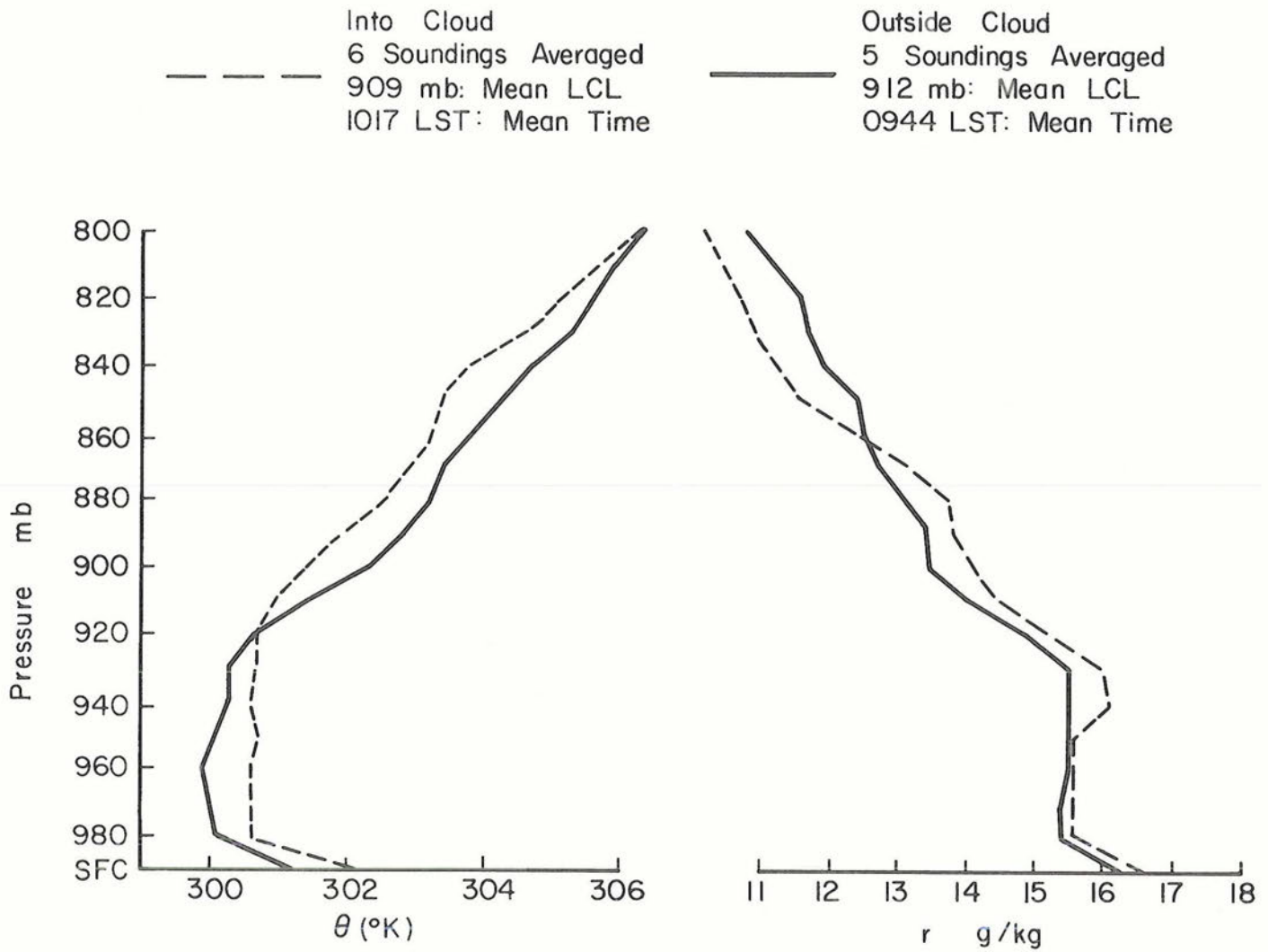

Figure 3.7: Mean outside-cloud (solid line) and into-cloud (dashed line) potential temperature (θ) and mixing ratio (r) profiles for soundings with mean L.C.L. between 910-920 mb.

We conclude that the air passing through cloudbase has properties closer to those of a 'mixed' subcloud layer than that of the surface air.

For the clear cases, the air is apparently not as well mixed below the LCL. Since mixing is not as great as that below cloud, the top of the mixed layer is not as distinct and the stable transition zone is visible.

A very weak (0.1^{o} K) θ-minimum is seen at 940 on the average of clear air ascents and at 960 mb. on the average of those soundings that entered cloud.

Above the LCL, the "into-cloud" average profiles are cooler up to 830 mb. and more moist up to 810 mb. Above these levels, there is little difference in structure between the two averages.

3.3 Determination of the Surface Energy Flux

3.3.1 Dependence of Dry Convection on Surface Energy Fluxes

The energy which drives the dry convection is the net radiation received at the earth's surface. Some of the energy is conducted into the soil while the remainder enters the lower atmosphere in the form of sensible and latent heat. The flux of energy from the surface determines the structure in the dry convective layer above. In order to study the time dependence of structural features in the dry convective layer, the time variation of the surface energy fluxes must first be known.

3.3.2 Surface Energy Balance

The energy balance at the surface of the earth consists of the following terms:

a) Net solar (short-wave) radiation

b) Net terrestrial (long-wave) radiation

c) Turbulent transport of sensible heat ($\rho c_p \overline{w'\theta'}$) into the atmosphere

d) Turbulent transport of latent heat ($\rho L \overline{w'r'}$) into the atmosphere

e) Conduction of heat into the soil

3.3.3 Net Radiation

The net radiative flux at the surface (terms A and B) must be accounted for by the remaining three terms.

Hourly measurements of net (short and long wave) radiation at the surface were taken on 57 of the 108 days during which VIMHEX II was in progress. As might be anticipated, the overall average of these data (Figure 3.8) shows a relatively uniform loss of energy from the earth's surface between 1930 and 0530 LST. An average of 2.4 langleys hr^{-1} in the form of long-wave terrestrial radiation enter the atmosphere during this period. After sunrise the downward flux of short wave energy increases at an average rate of 7.4 langleys hr^{-2} reaching a maximum value of +49.8 langley hr^{-1} at about 1230 LST. The average value of the net flux between 1130 and 1330 LST is +48.6 langleys hr^{-1}. After 1330 LST, the net radiation decreases (-7.5 langley hr^{-2}) to a value of -2.61 langleys hr^{-1} at 1930 LST.

Monthly averages of the radiation data were also constructed (Figure 3.9). The differences between the June, July and August curves between 0900 and 1500 LST may be attributed to: (1) the

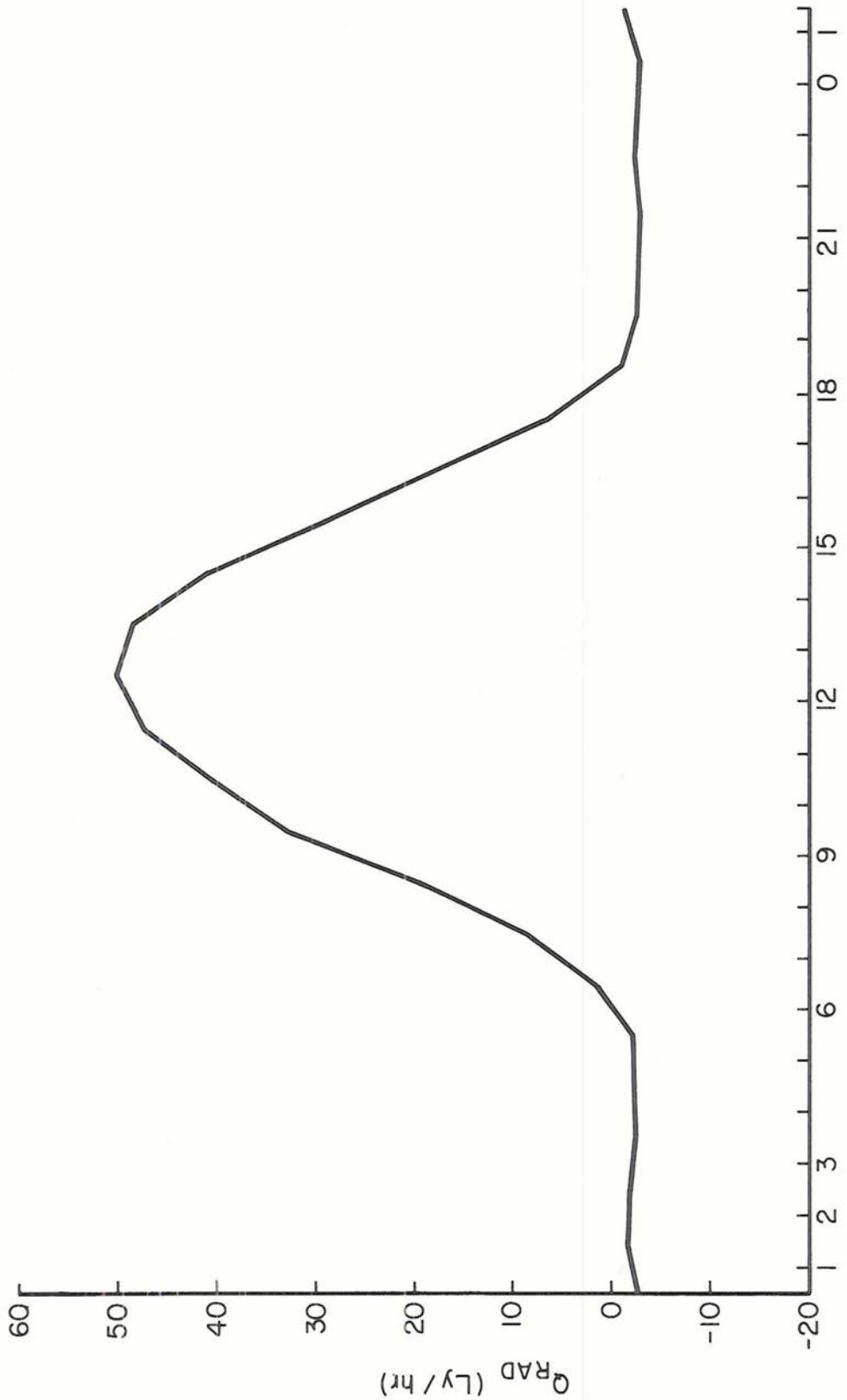

Figure 3.8: Average of all VIMHEX II net radiation data.

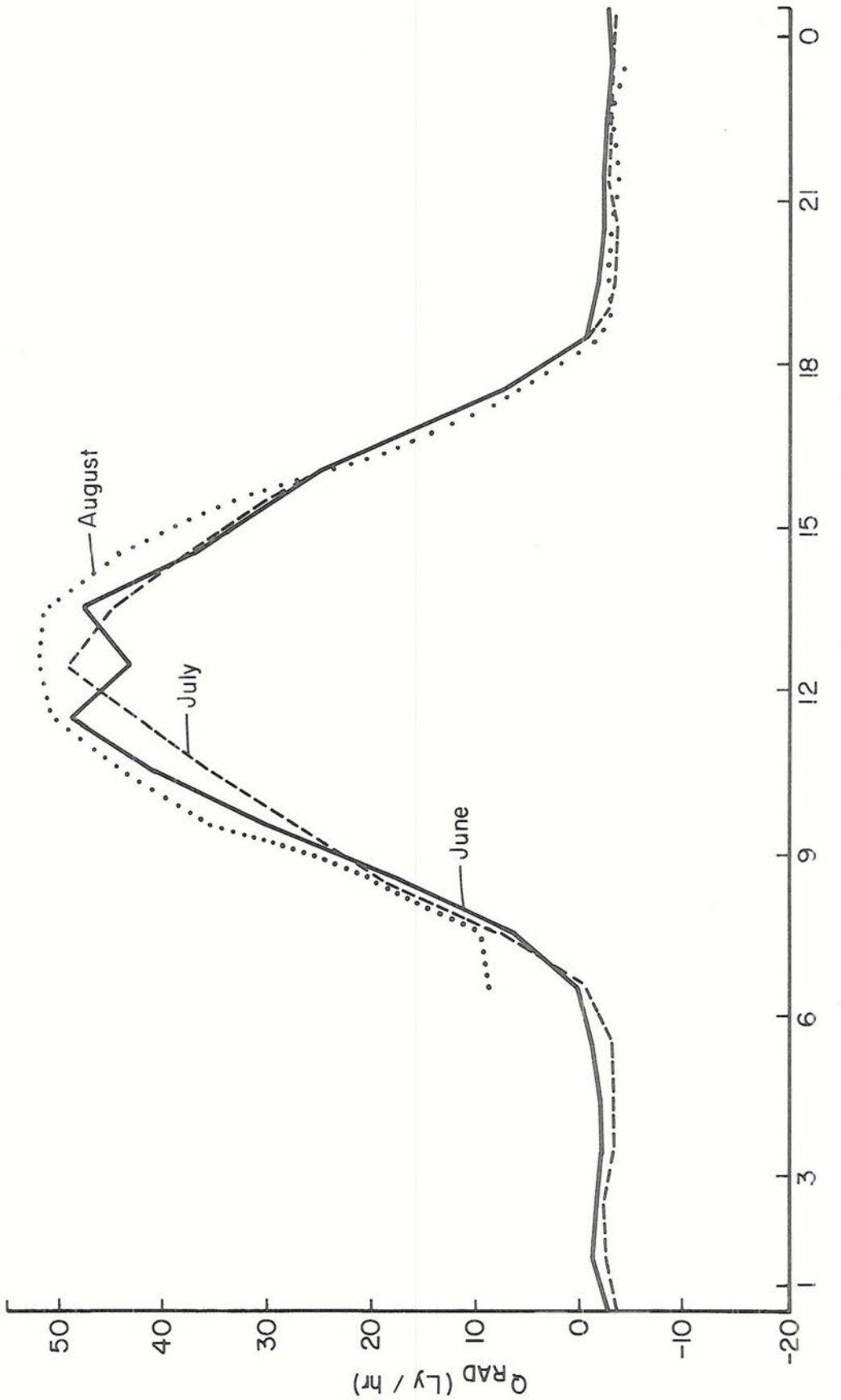

Figure 3.9: Monthly averages of VIMHEX II radiation data.

difference in the data sample size for each month (June - 7 days; July - 22 days; August - 28 days), and (2) variation in mean cloudiness. A particularly notable feature is the pronounced minimum in the June curve. Although the data sample for June is small, this depression in the net radiation curve indicates the presence of a well-defined diurnal maximum of cloudiness.

Using the previously described categorization of each day of the experiment according to the intensity of convection, net radiation curves were obtained for the relatively cloudless (Category I) days and the relatively cloudy (Category IV) days (Figure 3.10).

3.3.4 Soil Conduction

a) The energy balance at the earth's surface described in 3.3.2 may be written as follows:

Net radiation - heat conducted into soil = latent heat + sensible heat (3.1)

The objective of this section is the determination of the sensible and latent heat fluxes from the surface into the sub-cloud layer. Something, therefore, must be said about the amount of heat conducted into the soil.

b) There were measurements of soil heat content taken on seven days during the experiment. The total heat content of a layer of soil is given by:

$$H = \Sigma H_i = \Sigma C_o W_{si} (T_i - T_o) t_i \qquad (3.2)$$

where:

i = identifies each sub-layer comprising the total layer

C_o = the specific heat of the soil including air and water

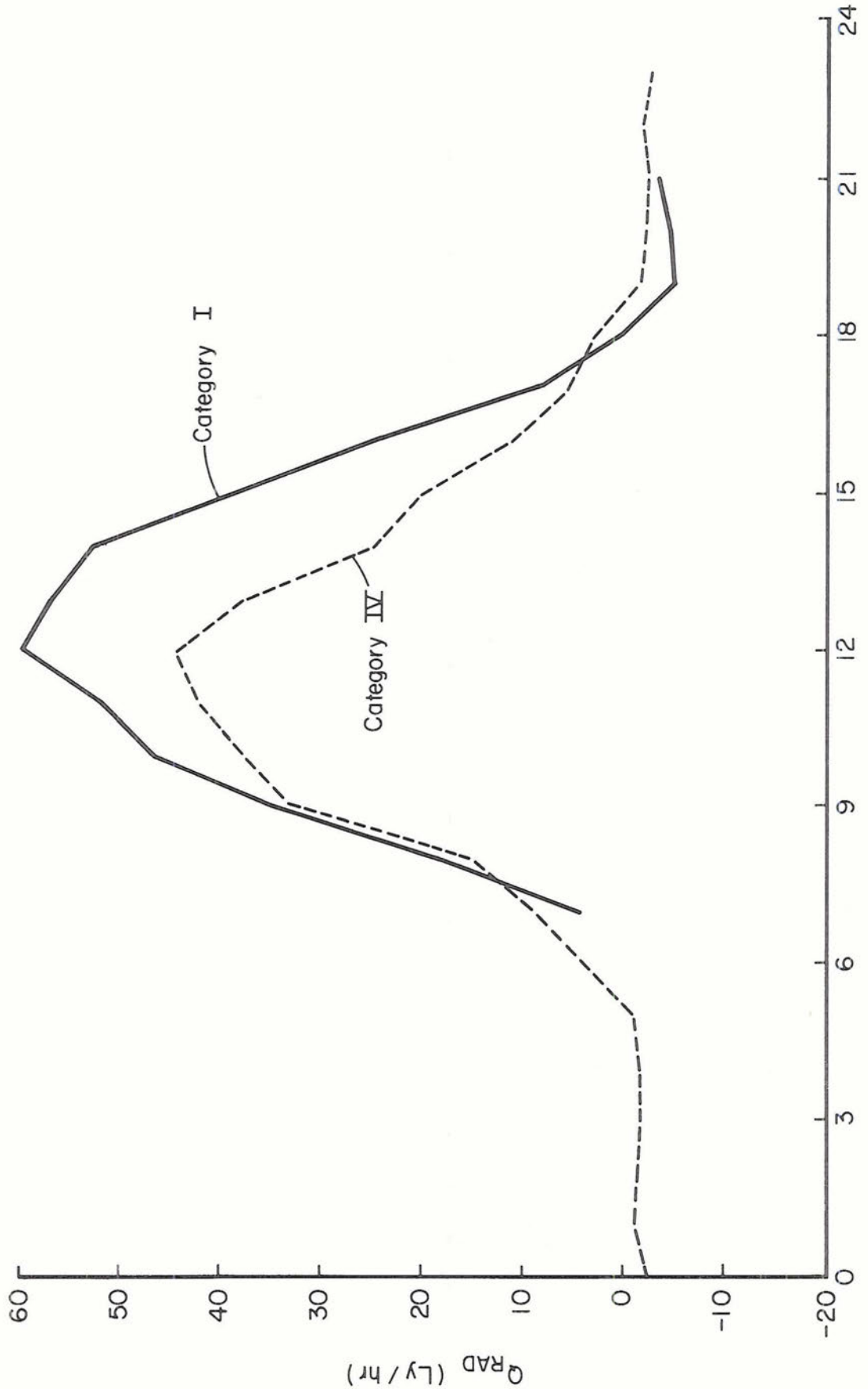

Figure 3.10: Average radiation for Category I & II days.

W_s = the dry unit weight of the soil (gm/cm^3)

T_i = mean temperature of the sub-layer

T_o = reference temperature

t = layer thickness

Thermocouples were placed at 0, 2, 4, 6, 10, 20, 30, 40, 50 and 70 cm below the surface. The dry unit weight, W_s, of each layer between thermocouples were measured and C_o, the specific heat of the soil was calculated to be 0.33 cal gm^{-1} $^oC^{-1}$ assuming a soil moisture content of 15%. T_o was arbitrarily chosen to be 30^o C.

c) Five of the days on which these measurements were taken fell into Categories I and II, i.e., relatively dry days, while the remaining two days were relatively wet. Figure 3.11 shows the time variation of the soil heat content for the five "dry" days.

Table 3.1 gives the average hourly values of the heat flux through the soil on a "dry" day between 0600 and 2400 LST. The data are also shown on Figure 3.12.

Since dry convection is the principal area of interest in this investigation, only the soil conduction data for these dry days will be used.

3.3.5 Average Surface Sensible and Latent Heat Fluxes

The average latent and sensible surface heat fluxes have been calculated by subtracting the average heat flux through the soil from the average net radiation for the dry days. The results are tabulated (Table 3.2) and are plotted on Figure 3.13.

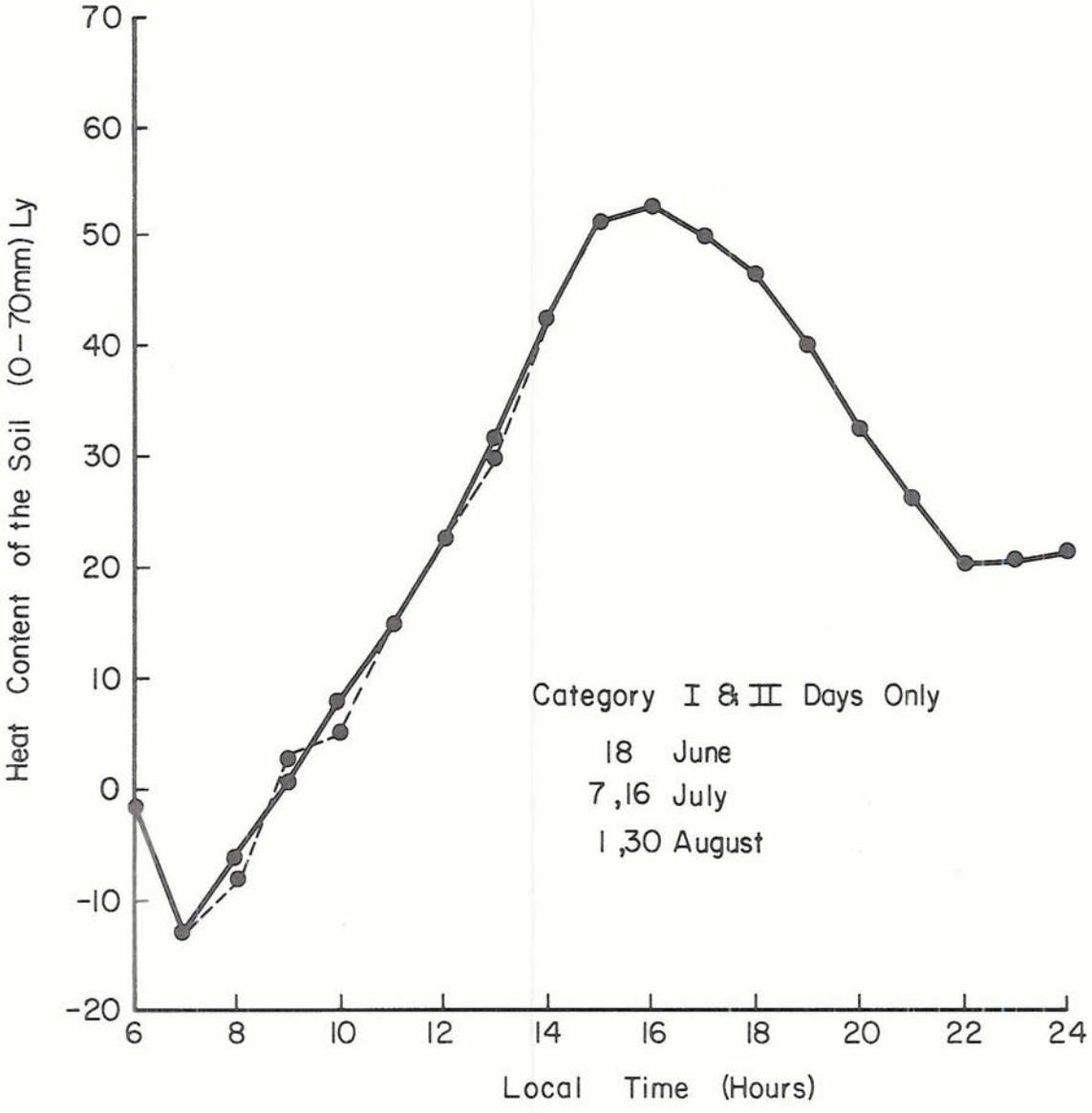

Figure 3.11: Soil heat content vs. time for Category I & II.

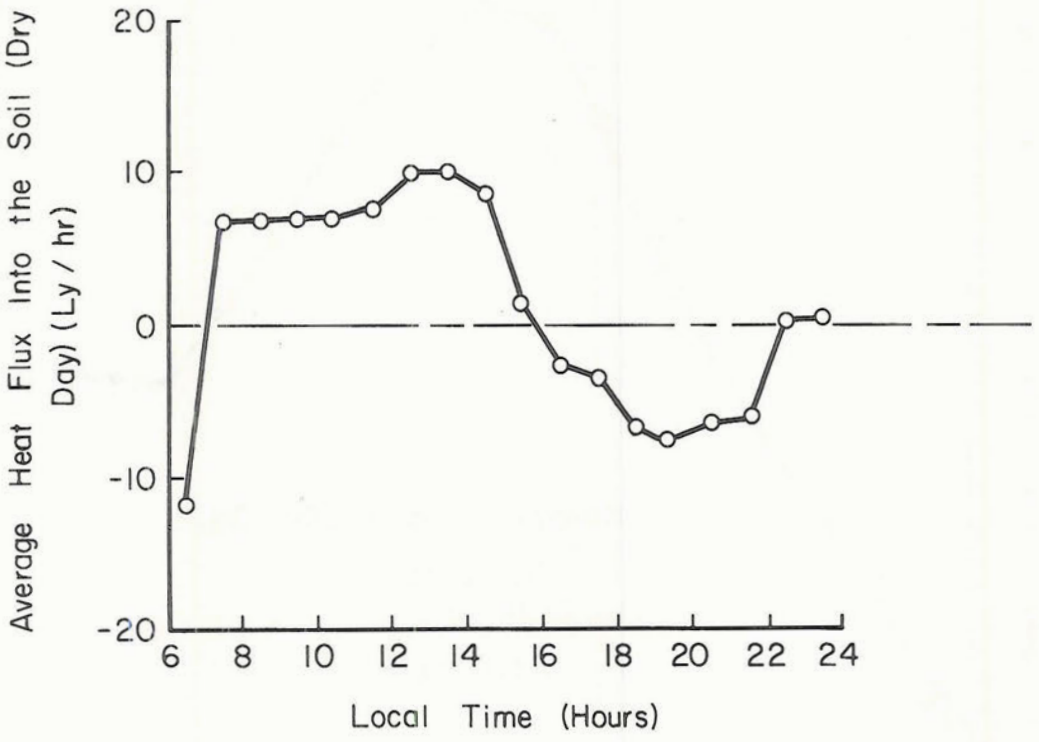

Figure 3.12: Mean heat flux into the soil for Category I & II days.

TABLE 3.1

Heat conducted into soil on Category I & II days (Ly/Hr) (smoothed).

Local Time	06-07	07-08	08-09	09-10	10-11	11-12	12-13	13-14	14-15
Q_2	-12.90	-06.10	+0.80	7.75	14.86	22.60	32.51	42.43	51.08
$-Q_1$	1.45	12.90	+6.10	-0.80	-7.75	-14.86	-22.60	-32.51	-42.43
(Q_2-Q_1)	-11.45	+6.80	+6.90	+6.95	+7.11	+7.74	+9.91	+9.92	+8.65

Local Time	15-16	16-17	17-18	18-19	19-20	20-21	21-22	22-23	23-24
Q_2	52.56	49.97	46.52	40.11	32.55	26.24	20.23	20.49	21.20
$-Q_1$	-51.08	-52.56	-49.97	-46.52	-40.11	-32.55	-26.24	-26.23	-20.49
(Q_2-Q_1)	+ 1.48	-2.59	-3.45	-6.41	-7.56	-6.31	-6.01	+0.26	+0.71

Q(2400) - Q(0600) = 21.20 - (-1.45) = 22.65

Σ Negative Q's = -43.78

Σ Positive Q's = 66.43

Σ Positive Q's + Σ Negative Q's = 66.43 - 43.78 = 22.65

TABLE 3.2

Dry days - Category I

Net radiation - heat conducted into soil = latent heat + sensible heat.

Local Time	0700-0800	08-0900	09-10	10-11	11-12	12-13	13-14	14-15	15-16	16-17
Net Radiation	4.1	18.1	35.0	46.7	51.8	59.6	56.7	52.6	37.9	24.3
Heat Into Soil	+11.5	-6.8	-6.9	-7.1	-7.7	-9.9	-9.9	-8.7	-1.5	+2.6
LH + SH	+15.6	+11.3	+28.1	+39.6	+44.1	49.7	46.8	+43.9	+36.4	+26.9

Local Time	17-18	18-19	19-20	20-21	21-22
Net Radiation	8.2	-2.8	-5.0	-4.7	-3.5
Heat Into Soil	+3.5	+6.4	+7.6	+6.3	+6.0
LH + SH	+11.7	+3.6	+2.6	+1.6	+2.5

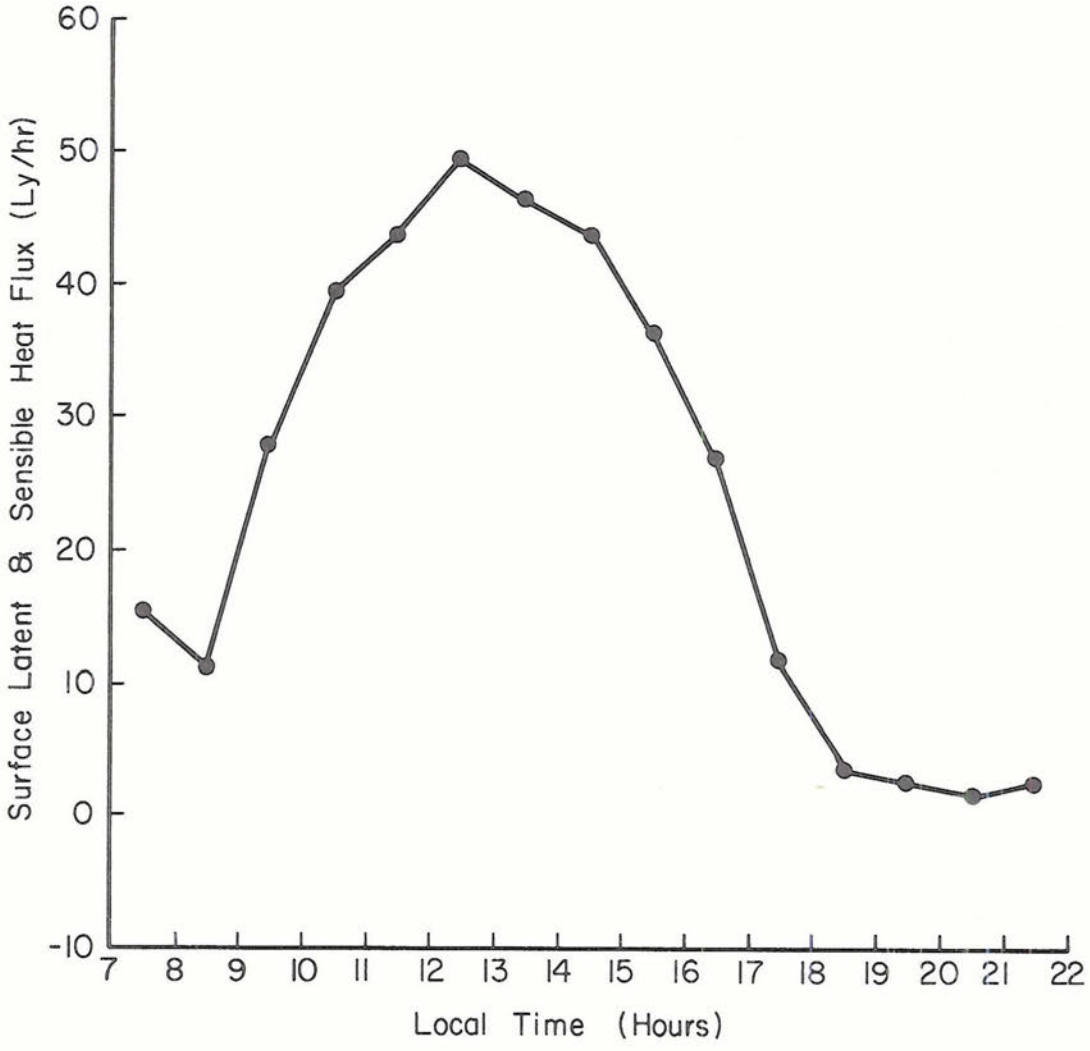

Figure 3.13: Mean surface sensible and latent heat flux for Category I & II days.

3.4 Time Dependence of the Dry Convective Layer Structure

3.4.1 General Considerations

The purpose of section 3.2 was to establish the existence of certain characteristic features of dry convective structure in the averaged VIMHEX II data and to learn something about the relation of the features to each other.

The next step, after establishing the fact that there is a "typical" dry convective structure, is to investigate the evolution of that structure during the day. For the investigation of structure, the soundings were grouped according to structure, i.e., by LCL. The emphasis of this section is on time variations and so the soundings will be grouped according to time (see Section 2.7.2).

Three separate sets of data will be used. They are:

a) 118 Category I and II (dry) soundings which have a 25 mb. vertical resolution. These soundings will be difference averaged (Section 2.7.4). The average profiles obtained from this data are not expected to show detailed structure but rather to indicate the major changes which occur in the layer during the day.

b) 112 non-precipitating convective soundings with 10 mb. vertical resolution which did not enter cloud. These will be vertically scaled by the height of the LCL so that structural features will be retained in the time averages.

c) Twenty soundings with 25 mb. vertical resolution which were taken during five of the "dry day" experiments conducted

as part of VIMHEX II. These will be difference averaged and used in the study of the time dependence of the layer.

It is important to consider how the data was selected for each of three sets. Category I and II soundings were selected on the basis of areal mean precipitation. Soundings taken when precipitation was occurring at or near Carrizal are included if the mean precipitation over the area is less than 2.0 mm. The remaining two data sets were selected on the basis of "dry" structure. Since precipitation causes marked changes in structure (Section 4), soundings taken during or near precipitation were systematically excluded. The Category I and II mean profiles represent slightly wetter and cloudier conditions than the mean profiles obtained from either of the other two data sets.

The θ-, r- and θ_e-structure will be studied in turn, using mean profiles obtained from the three data sets. The mean profile for a particular time period will be shown by a solid line and the mean profile for the next time period shown by a dashed line. This allows the changes which occur from one period to the next to be seen more easily. The initial profile will be plotted (dotted line) in the final diagram of each figure to show the net change which occurs during the day. Solid horizontal lines are used to mark the top of the surface layer (975 mb.) and the LCL.

3.4.2 Category I and II Difference Averaged Profiles

a) Thermal Structure (Figure 3.14): As anticipated (Section 2.7.4), most of the structural detail has been smoothed out.

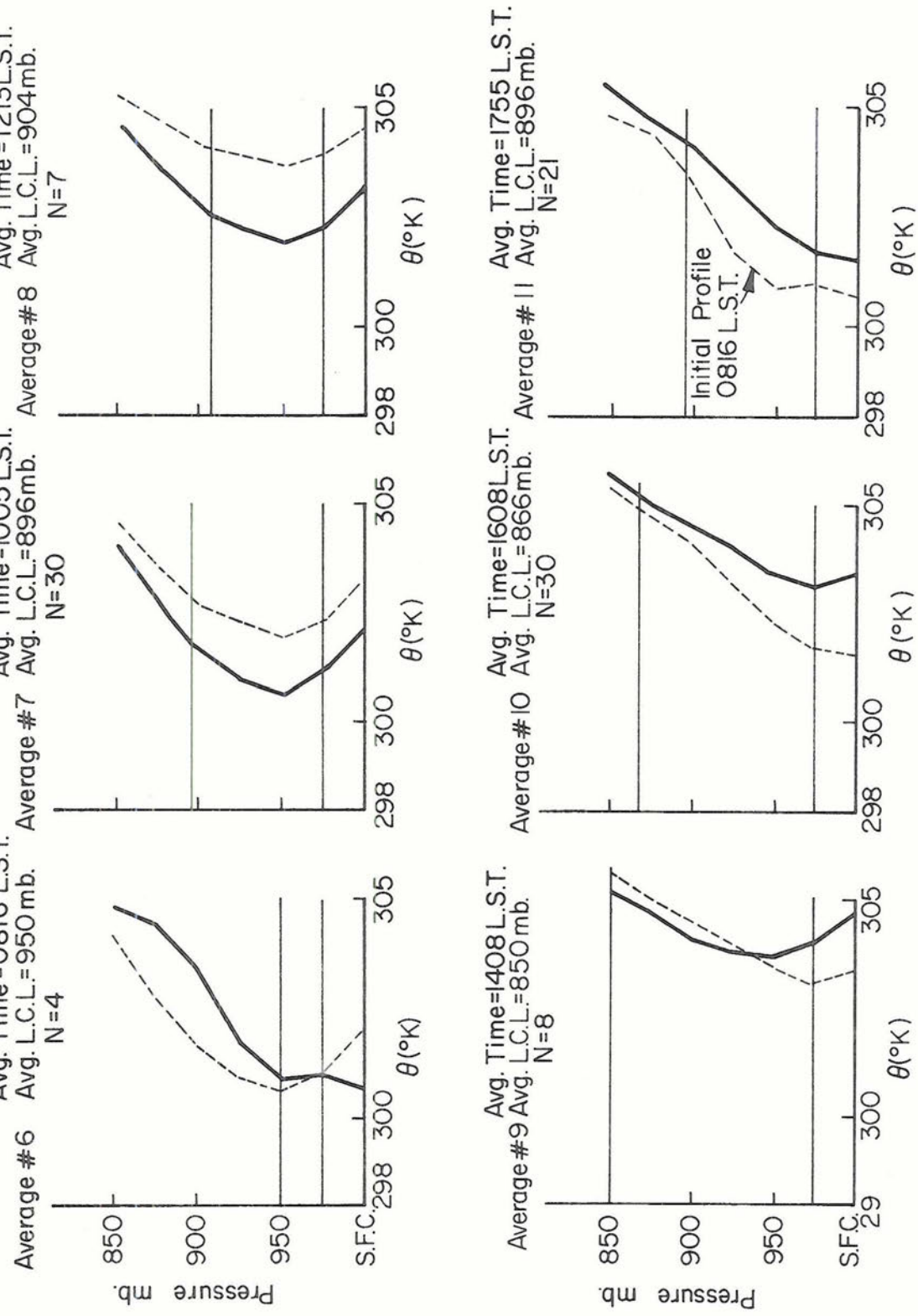

Figure 3.14: Time averages Category I & II potential temperature profiles.

There is some indication of a nocturnal surface inversion on the 0816 LST θ-profile which is not seen at 1005 LST. The atmosphere is seen to be unstable up to 950 mb. and stable above 950 mb. from 1000 LST through 1400 LST. After 1400 LST, the decrease in the potential temperature near the surface increases the stability of the lowest layers and by 1800 LST the entire lower atmosphere has been stabilized. This is probably due to precipitation on some of the days included in this sample (see Section 4.3). The LCL increases from 950 mb. at 0816 LST to a maximum of 850 mb. at 1408 LST after which it begins to decrease in height.

b) Moisture Structure (Figure 3.15): Moisture decreases rather uniformly between the surface and the LCL. The decrease averages about 3.0 gm kg^{-1}. It is difficult to infer much about physical processes leading to the redistribution of moisture in the dry convective layer due to the alternating increases and decreases in moisture content which are indicated at each level. These profiles do not show any evidence of abrupt changes in the rate of decrease of moisture with height.

c) θ_e Structure (Figure 3.16): The θ_e content of the dry convective layer increases throughout most of the period during which convection is occurring. The surface θ_e reaches its maximum value near 1200 LST. Two significant changes in decrease of θ_e with height are observed. The first occurs at 950 mb. and is probably related to the change in the thermal stability which occurs at this same level (Figure 3.14).

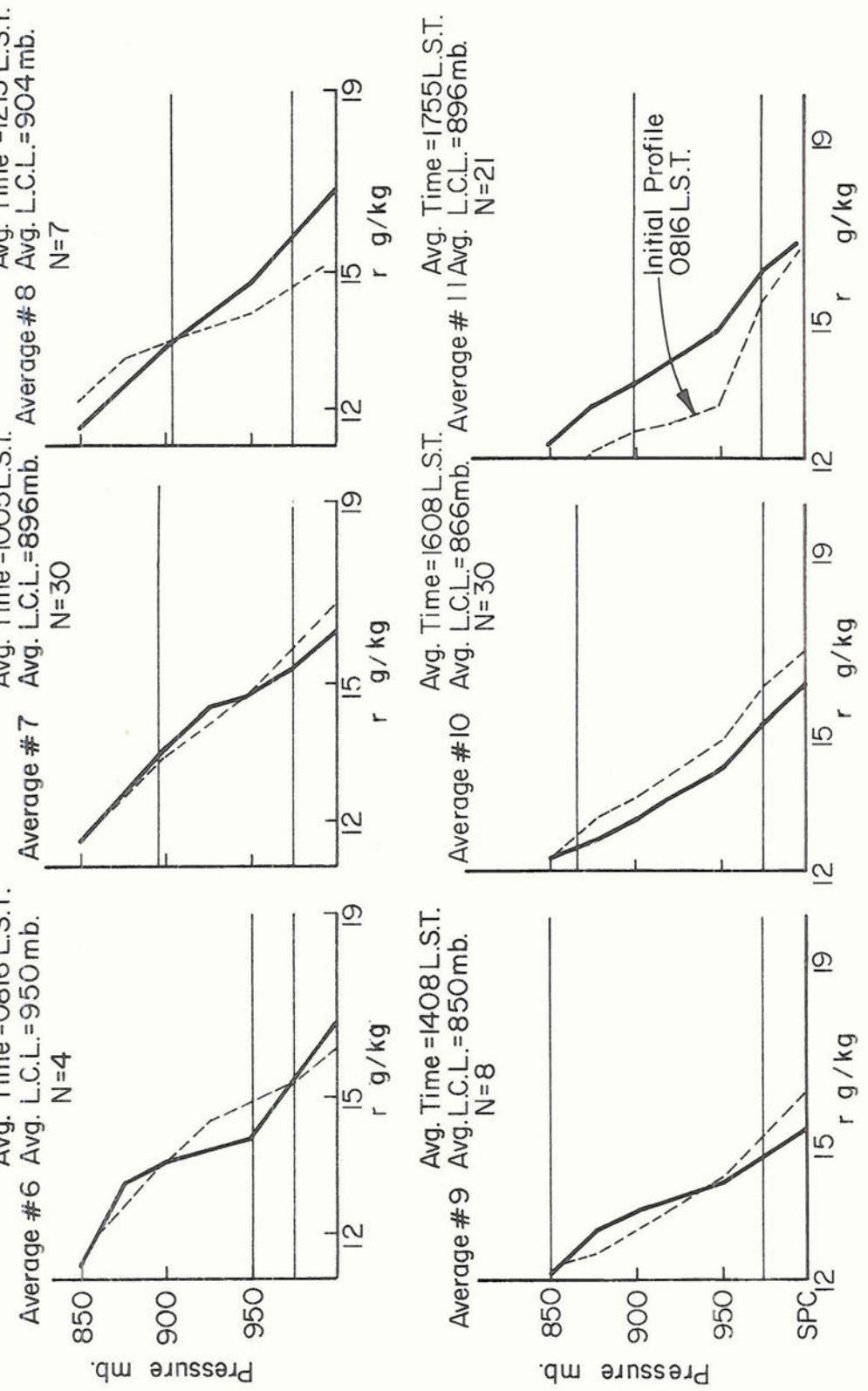

Figure 3.15: Time averaged Category I & II mixing ratio (r) profiles.

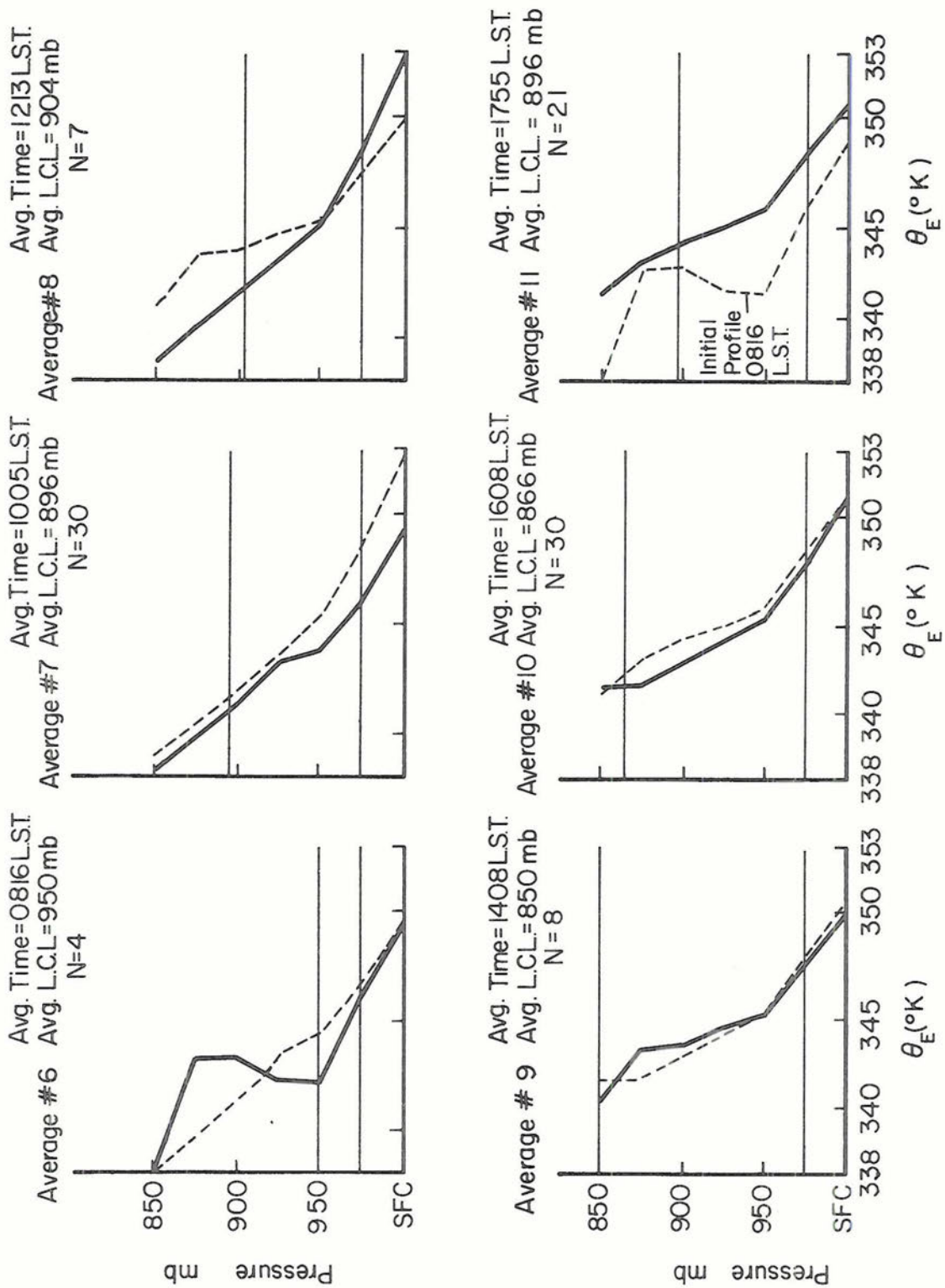
Average #6
Avg. Time=0816 L.S.T.
Avg. L.C.L=950 mb
N=4
Average #7
Avg. Time=1005 L.S.T.
Avg. L.C.L.= 896 mb
N=30
Average#8
Avg. Time=1213 L.S.T.
Avg. L.C.L.= 904 mb
N=7
Average # 9
Avg. Time=1408 L.S.T.
Avg. L.C.L.= 850 mb
N=8
Average #10
Avg. Time=1608 L.S.T.
Avg. L.C.L.=866 mb
N=30
Average #11
Avg. Time=1755 L.S.T.
Avg. L.C.L. = 896 mb
N=21
Initial Profile 0816 L.S.T.
Pressure mb
850
900
950
SFC
338 340 345 350 353
θ_E(°K)

The second is observed 25 mb. below the LCL on the 1005 LST and 1408 LST mean profiles and corresponds to a slight change in the vertical moisture structure.

3.4.3 LCL-Scaled Dry Convective Average Profiles

a) Thermal Structure (Figure 3.17): Structural features are considerably better defined in this set of mean profiles. The large (1.0-1.5^{o} K) θ-decrease near the surface is found below P* = 0.15. Above this marked superadiabatic region, the air is initially stable but becomes neutral or slightly unstable during the day. This instability is most noticeable on the 1144 LST mean profile when it extends more than half-way up to the LCL. The variation in height of the θ minimum is shown in Figure 3.23.

On the 0838 LST mean profile, convection is just beginning and only the layer below P* = 0.35 is well mixed. That convection does not always extend up to the LCL early in the day is confirmed by the fact that cumulus clouds are not always observed at 0830 LST. In each of the subsequent mean profiles mixing extends upward and by 1545 LST the entire layer below P* = 0.95 has been relatively well mixed.

The potential temperature below the LCL in the dry convective layer increases throughout the period. However, this pressure-scaled data is not suitable for a discussion of the time changes of a variable at a pressure level. This will be done in Section 3.4.4.

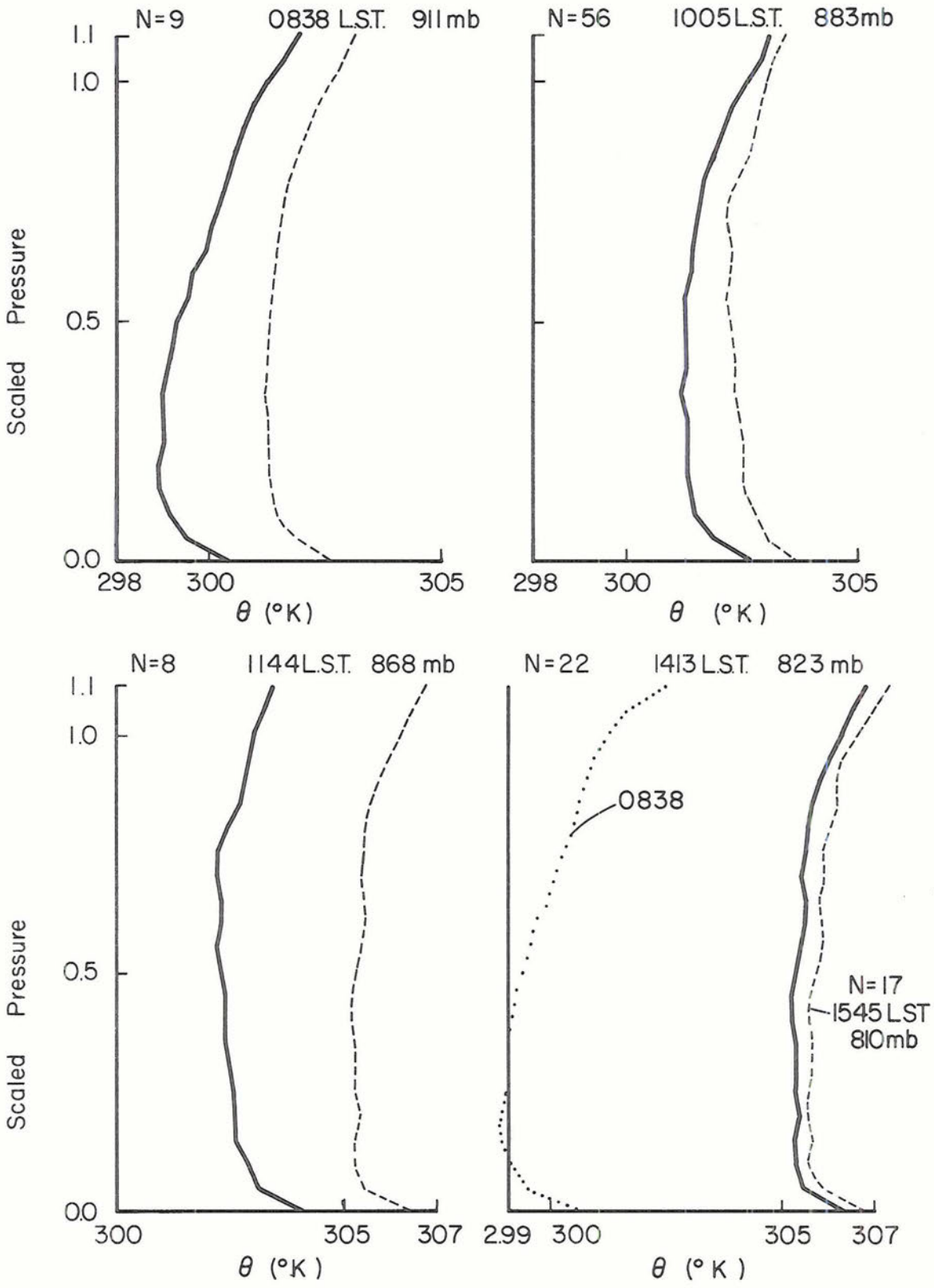

Figure 3.17: Time averaged, LCL-scaled, dry convective θ-profiles.

b) Moisture Structure (Figure 3.18): There is a 1.0-1.5 gm kg^{-1} decrease in mixing ratio between the surface and P* = 0.1 during the morning but by 1200 LST the decrease through this layer is less than 1.0 gm kg^{-1}. The mixing ratio decreases gradually with height throughout most of the remainder of the layer. A change in the rate of decrease occurs near the top of the layer (between P* = 0.75 and P* = 0.90). The top of the water vapor "mixed" layer is, therefore, comparable with the top of the thermal mixed layer.

c) θ_e Structure (Figure 3.19): The 0838 LST mean θ_e-profile shows a large (~ 6.0°K) decrease between the surface and P^* = 0.15. This feature weakens on each successive profile and by the end of the period (1545 LST) it has been reduced to about 3.0°K.

Above the surface layer θ_e is observed to increase with height only on the initial profile, before convection has become well established. The vertical structure is smooth at 0838 LST and 1005 LST, becomes irregular at 1144 LST and 1413 LST and perhaps begins to smooth out again at 1545 LST. Although it is possible that these irregularities are due to "noise" in the measurements, the smoothness of the early profiles suggests that the irregularities may be physically significant. Possibly, as the layer deepens, the structure of the dry convective eddies may change, but no firm conclusions can be drawn from this data as the data sample for each profile is different.

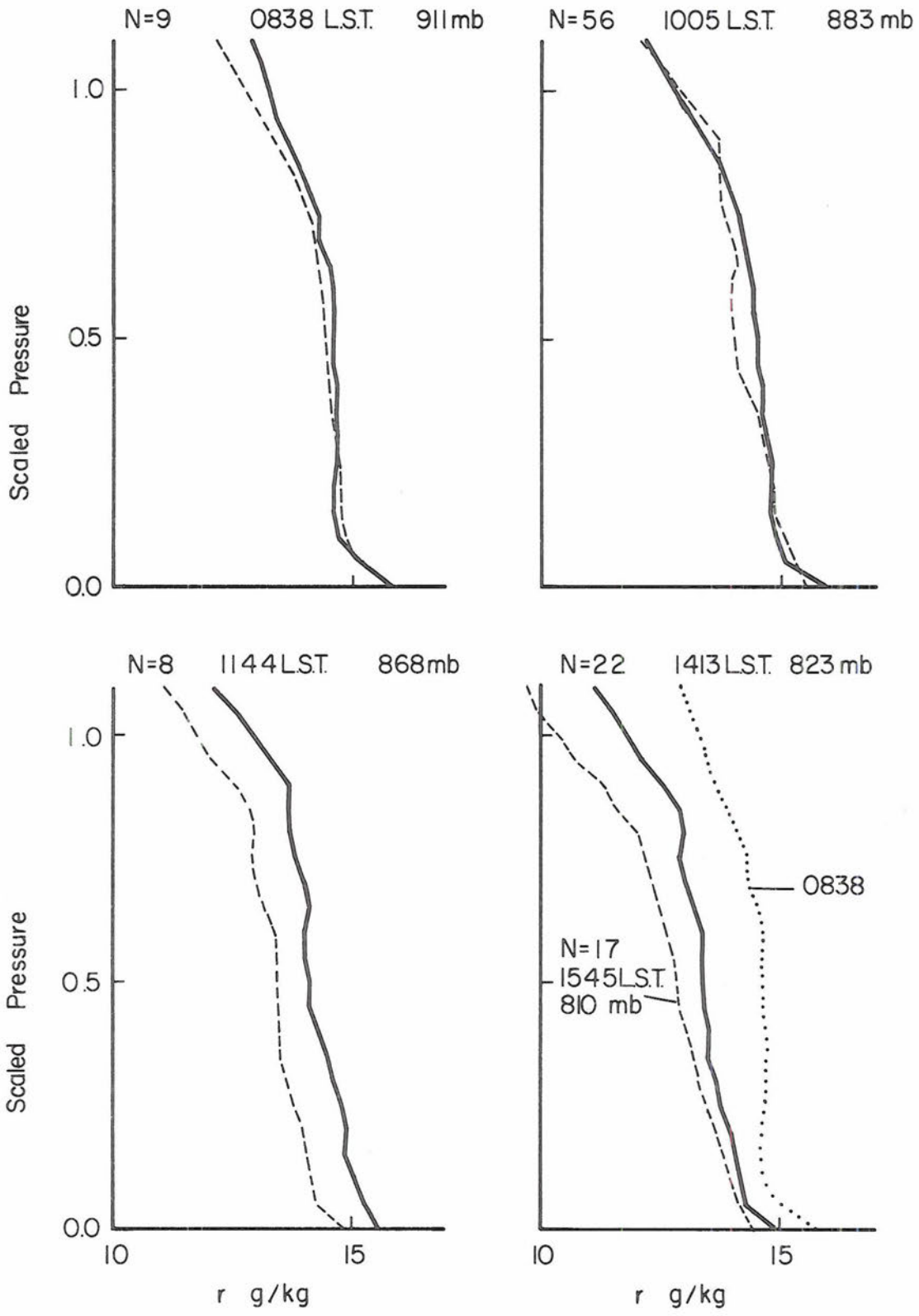

Figure 3.18: Time averaged, LCL-scaled, dry convective r-profiles.

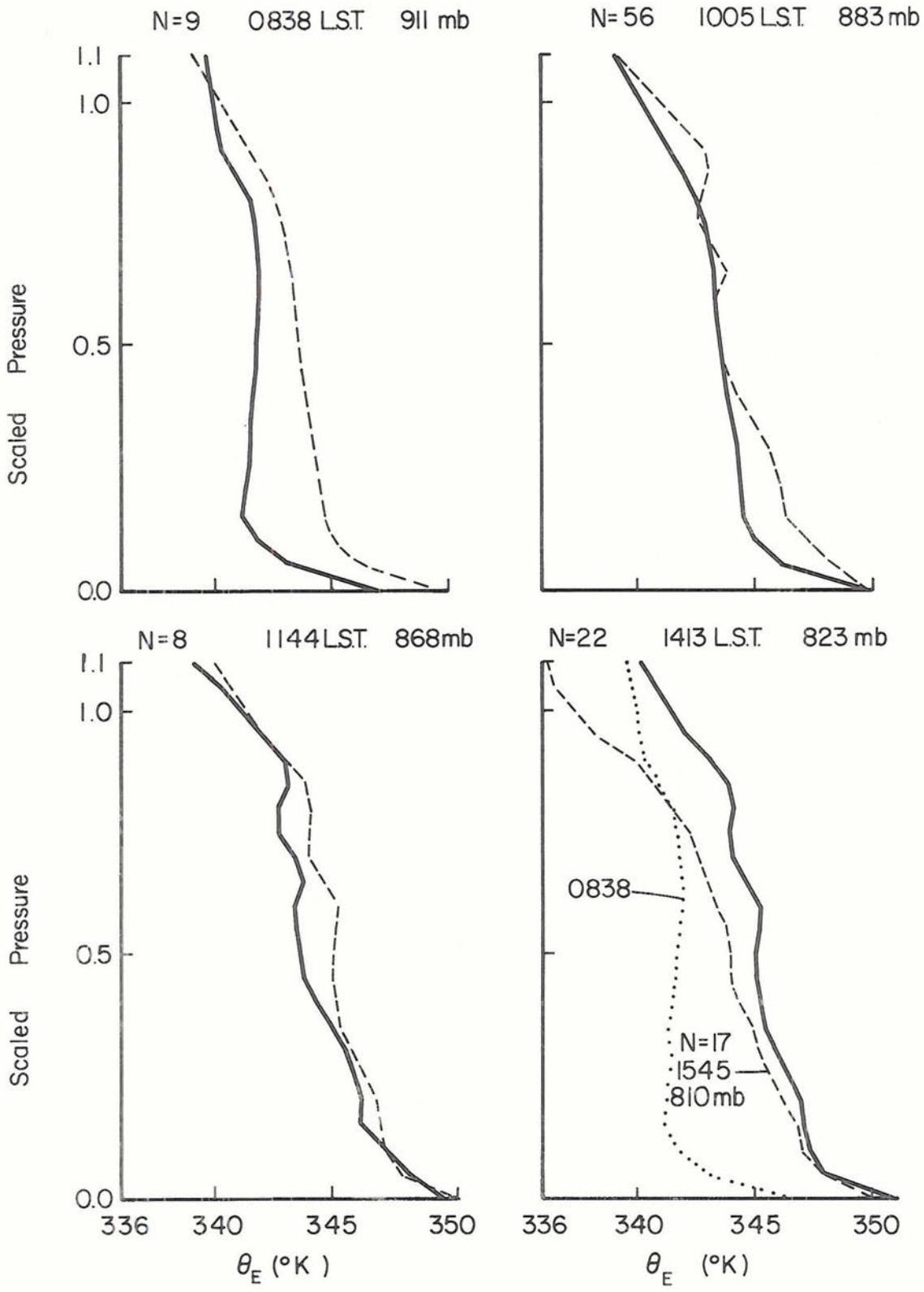

Figure 3.19: Time averaged, LCL-scaled, dry convective θ_e profiles.

At the top of the layer θ_e is seen to begin to decrease more rapidly with height between P* = 0.8 and P* = 0.9 in response to the presence of lower θ_e air above the dry convective layer.

3.4.4 "Dry-day Difference-average Profiles

a) Thermal Structure (Figure 3.20): The thermal structure shown on Figure 3.20 is similar to that obtained from the previous two sets of data. The strongly superadiabatic region above the surface extends up to 950 mb. except on the 1201 LST profile where it is as high as 925 mb. The mixed layer develops as indicated previously, almost reaching the LCL at 1600 LST. The entire dry layer warms throughout the period of observation. The maximum amount of heating is observed to occur between 1006 LST and 1359 LST.

b) Moisture Structure (Figure 3.21): This set of data is considered to be more representative of dry convection than that used in Section 3.2.2 since days when precipitation occurred were specifically excluded. Moisture is seen to decrease with height throughout the layer on each profile. The mixing ratio increases at each level above 975 mb. between 1000 LST and 1200 LST. Between 1200 LST and 1600 LST the amount of moisture at each level below 875 mb. decreases. The convection results in a drying out of the air below 875 mb. and a moistening of the air between 875 mb. and 800 mb. in the course of the day.

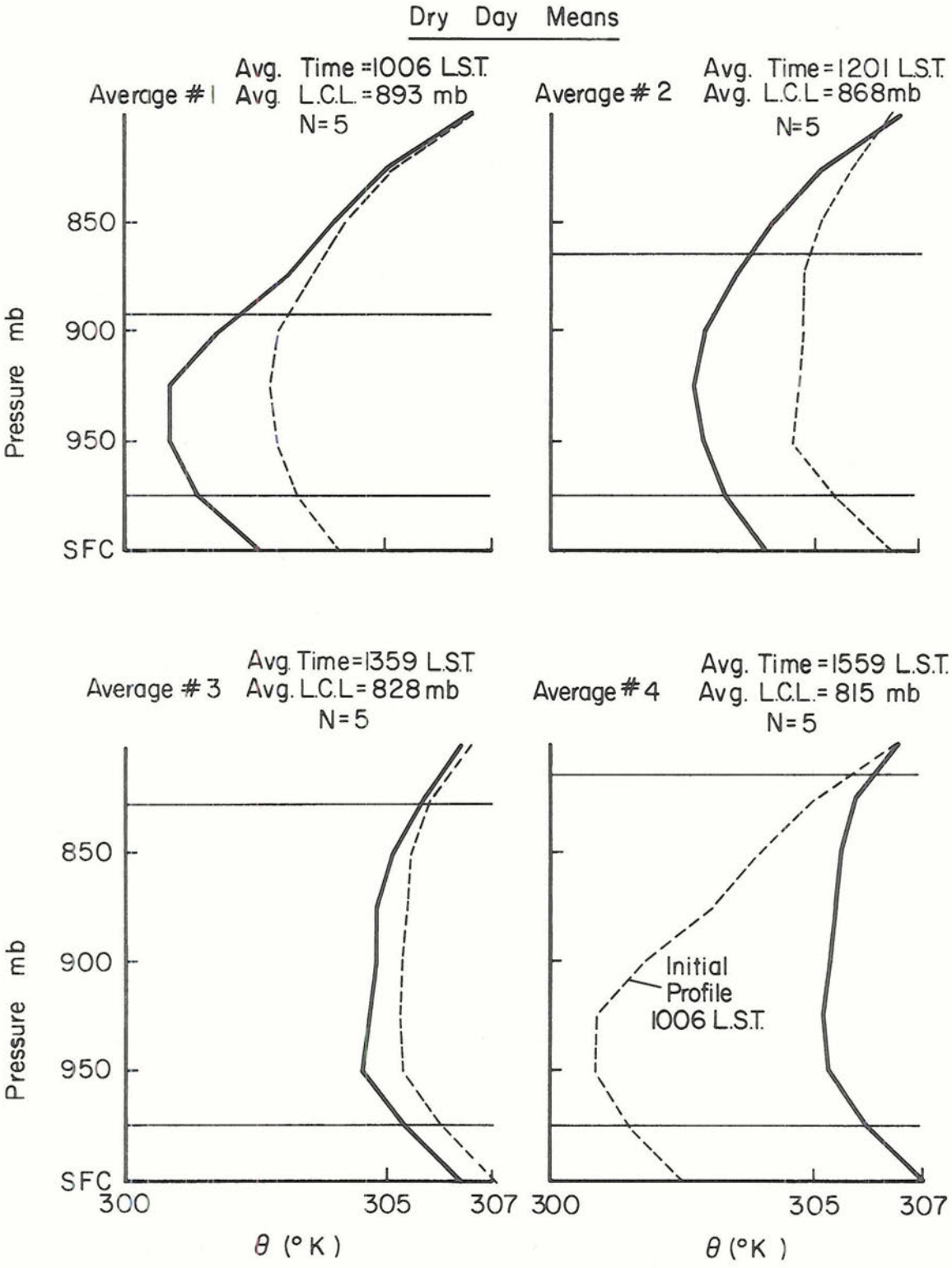

Figure 3.20: Difference averaged "dry-day" θ-profiles.

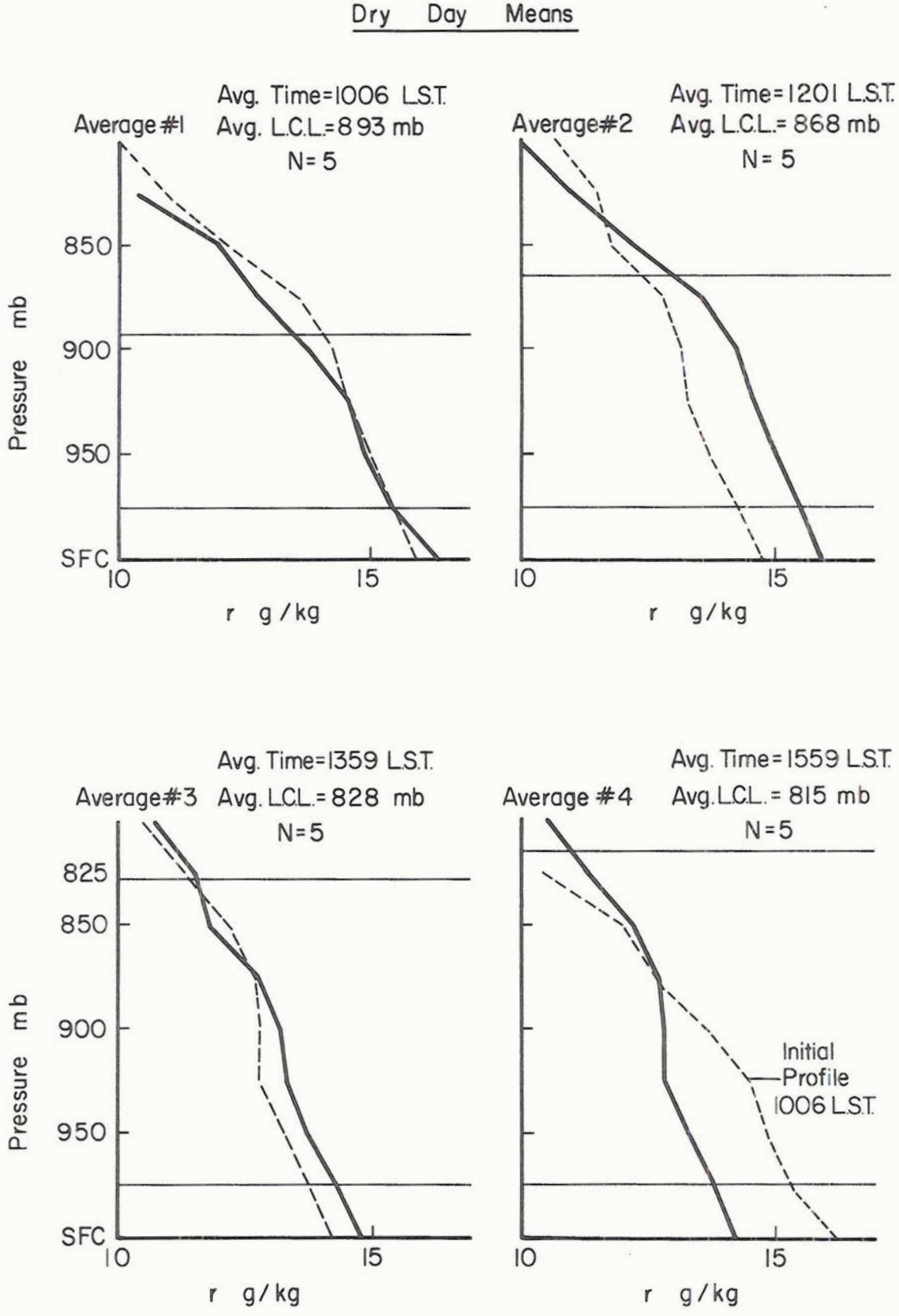

Figure 3.21: Difference averaged "dry-day" r-profiles.

c) θ_e Structure (Figure 3.22): The time dependence of the mean θ_e-profile reflects the redistribution of both sensible heat and moisture. Initially (1000 LST-1200 LST) θ_e increases throughout the layer. After 1200 LST θ_e is observed to decrease at most levels below the LCL. The total effect of dry convection through the day is to cause practically no change in the θ_e structure below 925 mb. but to increase the θ_e content of the layer above 925 mb. and below the final LCL, corresponding to the increase in depth of the dry convective layer.

3.4.5 Summary

These results are summarized on Figure 3.23 where the variation of several of the features of the thermal structure of the dry convective layer is shown. The data are presented in Table 3.3.

3.4.6 Surface Fluxes

a) θ_e Flux

The θ-minimum observed on several of the mean θ-profiles (Figures 3.14, 3.17, and 3.20) indicates that the lower portion of the mixed layer is thermally unstable. If this is so, then the magnitude of the surface sensible heat flux may depend on the decrease of θ through the entire unstable region, and not just through a surface layer with a fixed upper boundary.

The magnitude of the surface sensible and latent heat flux has been computed (Section 3.3.5). The time variation

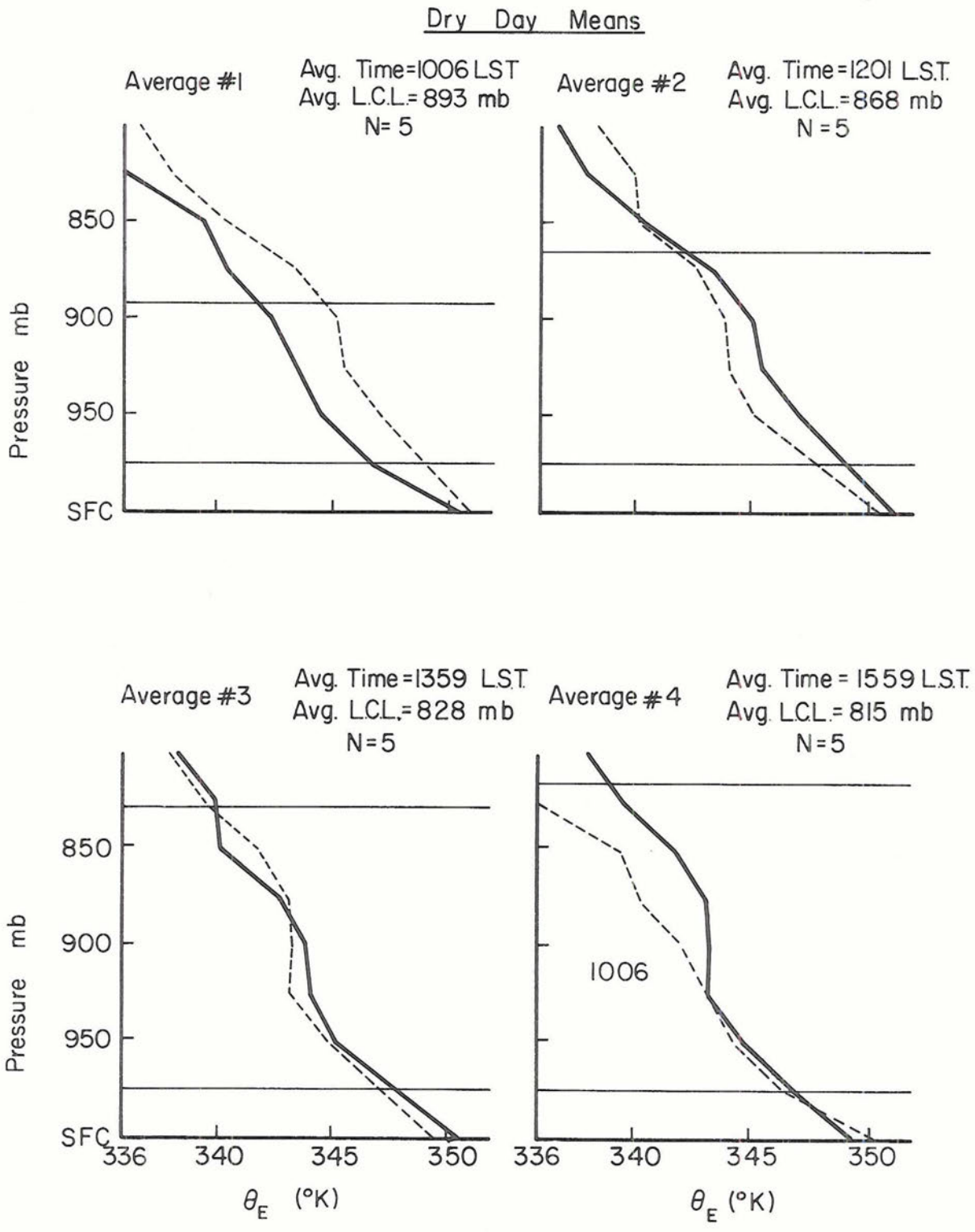

Figure 3.22: Difference averaged "dry-day" θ_e-profiles.

TABLE 3.3

	Time Interval	07-09	09-11	11-13	13-15	15-17	17-19	19-00
Category I & II Data	Average LST	0316	1005	1213	1408	1608	1755	2045
	# of Soundings	4	30	7	8	30	21	13
	Avg. Surface θ (^{o}K)	300.7	302.1	303.3	304.7	303.4	302.5	298.4
	Avg. $\Delta\theta$ (SFC-975 mb.) ^{o}K	-0.3	1.0	1.0	0.7	0.3	-0.2	-1.3
	Avg. Height of θ-Minimum (mb.)	950	950	950	950			
	Avg. Top of Mixed Layer (mb.)	950	925	900	900			
	Avg. $\Delta\theta$ (SFC-LCL) (^{o}K)	-0.2	+0.3	0.0	-0.5	-1.8	-2.7	-3.8
	Avg. LCL Height (mb.)	950	896	880	850	866	896	924
Scaled Data	Average LST	0338	1005	1144	1413	1545		
	# of Soundings	9	56	8	22	17		
	Avg. Surface θ (^{o}K)	300.5	302.8	303.9	306.4	306.9		
	Avg. $\Delta\theta$ (SFC-P*=0.1)(^{o}K)	1.3	1.3	1.0	1.1	1.4		
	Avg. Height of θ-Minimum (P*)	0.15	0.35	0.55	0.40	0.10		
	Avg. Top of Mixed Layer (P*)	0.35	0.65	0.75	0.85	0.95		
	Avg. $\Delta\theta$ (SFC-LCL) (^{o}K)	-0.7	+0.2	+0.9	+0.2	+0.4		
	Avg. LCL Height (mb.)	911	884	868	823	810		
Dry-day Data	Average LST		1006	1201	1359	1559		
	# of Soundings		5	5	5	5		
	Avg. Surface θ (^{o}K)		302.6	304.1	306.5	307.1		
	Avg. $\Delta\theta$ (SFC-975 mb.)(^{o}K)		1.1	0.8	1.1	1.1		
	Avg. Height of θ-Minimum (mb.)		935	925	950	925		
	Avg. Top of Mixed Layer (mb.)		925	900	850	825		
	Avg. $\Delta\theta$ (SFC-LCL) (^{o}K)		+0.4	+0.3	+0.9	+1.0		
	Avg. LCL Height (mb.)		893	868	828	815		

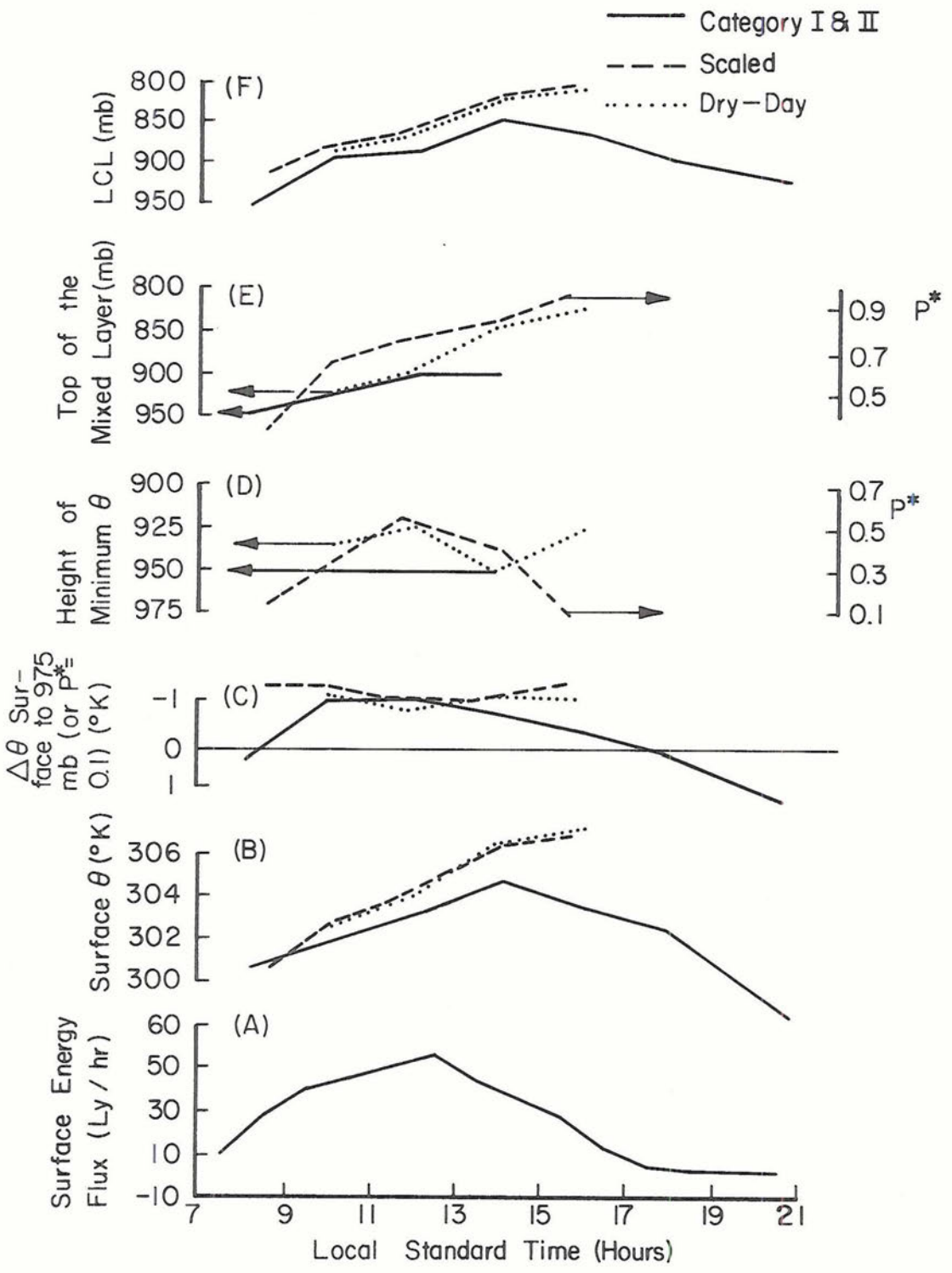

Figure 3.23: Time variation of selected mean dry convective layer features of the θ structure.

of the surface θ_e flux should correspond to the time variation of the computed surface sensible and latent heat fluxes, which can be calculated using a bulk aerodynamic equation:

$$F_{\theta_e} = C_{\theta_e} \tilde{\rho} (\theta_{e_o} - \theta_{e_t}) V_o \qquad (3.3)$$

where $\tilde{\rho}$ is the horizontally averaged air density

V_o is the surface wind speed ≃ constant

C_{θ_e} is a drag coefficient that probably increases a little with instability but which will be taken here as constant.

θ_{e_o} is the surface value of θ_e

θ_{e_t} is the value of θ_e at some level chosen as the top of the superadiabatic layer

Figure 3.24 and Table 3.4 show the variation with time of the difference between θ_{e_o} and four values chosen for θ_{e_t}. Also shown on Figure 3.24 is the surface energy flux computed from net radiation and soil heat measurements (Section 3.3).

Table 3.4: The variation with time of $\Delta\theta_e = \theta_{e_o} - \theta_{e_t}$ for four values of θ_{e_t} in the dry convective layer.

Local Standard Time $\Delta\theta_e$	07-09	09-11	11-13	13-15	15-17
1. Surface to P* = 0.1	2.5	2.3	1.2	1.8	1.7
2. Surface to P = 975 mb.		1.9	1.0	1.4	1.2
3. Surface to Average θ_e (P* = 0.1→0.8)	5.2	5.8	5.3	5.5	6.0
4. Surface to θ-Minimum	2.8	2.7	3.2	2.9	1.6

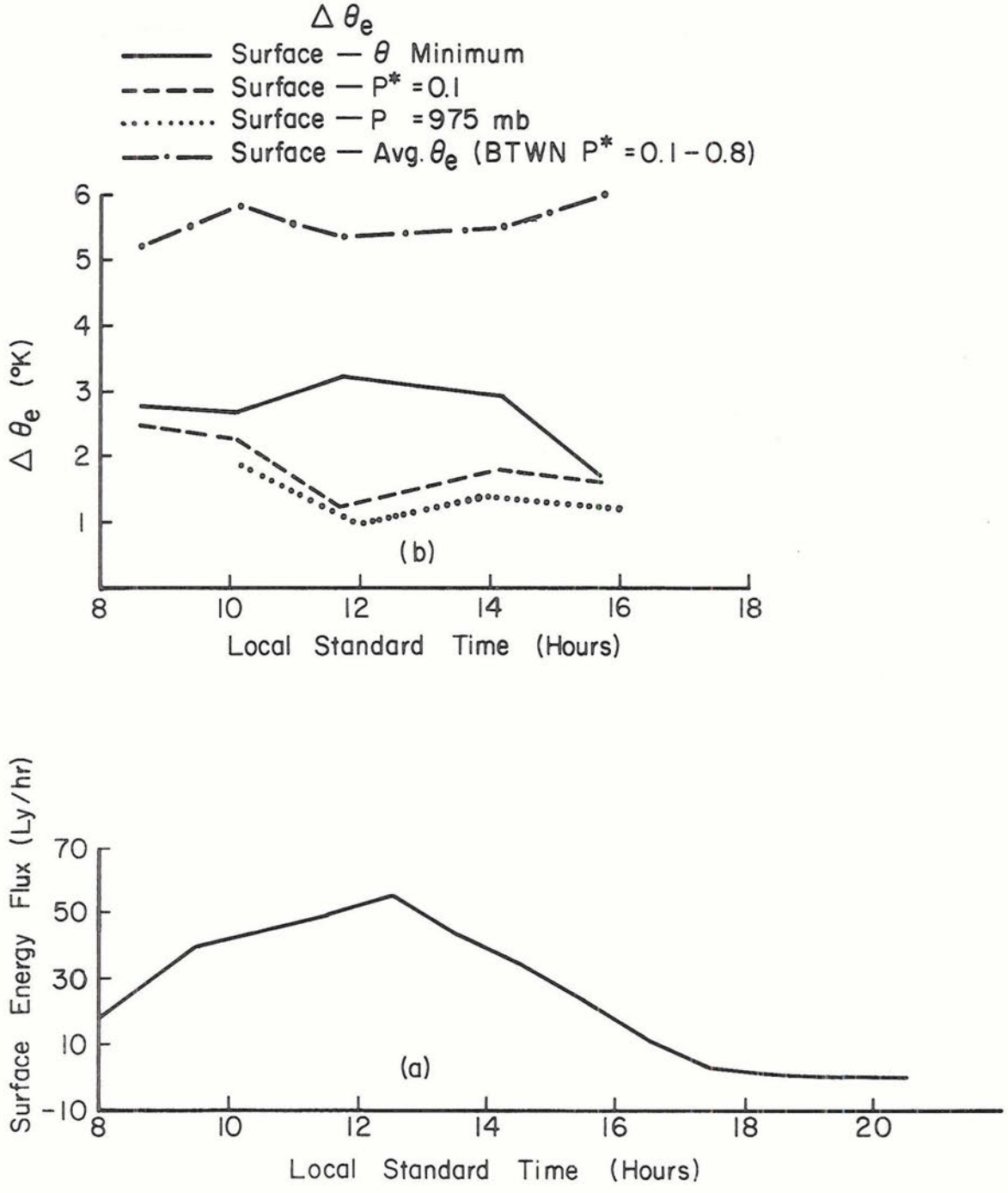

Figure 3.24: Time variation of the θ_e decrease in the lower portion of the dry convective layer.

There is little similarity in shape between the surface energy flux (Figure 3.24(a)) and the $\Delta\theta_e$ curves based on differences between the surface and P* = 0.1, P = 975 mb. or the average θ_e between P* = 0.1 and P* = 0.8. The agreement in shape with the $\Delta\theta_e$ curve computed from the surface to the level of the θ-minimum is reasonably good. This needs further study, but these data do not confirm that surface fluxes are well predicted by the bulk aerodynamic method using the difference between surface θ_e and a mean value for the mixed layer.

b) The Bowen Ratio

The surface sensible and latent heat fluxes are assumed to be given by bulk aerodynamic equations of the form:

$$F_{o_\theta} = C_\theta \tilde{\rho}_o C_p (\tilde{\theta}_o - \tilde{\theta}_t) V_o \qquad (3.4)$$

$$\text{and } F_{o_r} = C_r \tilde{\rho}_o L_v (\tilde{r}_o - \tilde{r}_t) V_o \qquad (3.5)$$

respectively, where V_o is the magnitude of the wind at some level in the superadiabatic layer, C_θ and C_r are essentially drag coefficients (assumed to be approximately equal) and θ_o, θ_t and r_o, r_t are the surface and top of the superadiabatic layer values of θ and r, respectively. The $\sim$ represents a horizontal average.

The existence of a θ-minimum in the mixed layer leaves some question as to where, exactly, the top of the superadiabatic layer is located. To investigate the significance of this feature in flux computations, the Bowen ratio was computed with $\tilde{\theta}_t$ and $\tilde{r}_t$ taken to be (as in 3.4.6(a)):

1) the values at P* = 0.1

2) the values at P = 975 mb.

3) the values at P* (θ minimum)

4) the mean $\tilde{\theta}$ and $\tilde{r}$ between P* = 0.1 to 0.8.

These data are shown on Table 3.5 and are plotted on Figure 3.25. The Bowen ratio has been computed using:

$$\text{Bowen ratio} = \frac{F_{o_\theta}}{F_{o_r}} = \frac{C_p}{L_v}\left(\frac{\theta_o - \theta_t}{r_o - r_t}\right) \qquad (3.6)$$

Table 3.5: The Bowen ratio computed using $\tilde{\theta}$ and $\tilde{r}$ differences between the surface and selected levels in the dry convective layer

LOCAL STANDARD TIME	07-09	09-11	11-13	13-15	15-17
1) Surface to P*=0.1					
$\Delta\theta$ (^oK)	1.3	1.3	1.0	1.1	1.4
Δr (gm kg^{-1})	1.2	1.0	0.5	0.7	0.6
Bowen ratio	0.44	0.53	0.82	0.64	0.96
2) Surface to P=975 mb.					
$\Delta\theta$ (^oK)		1.1	0.8	1.1	1.1
Δr (gm kg^{-1})		0.9	0.4	0.5	0.4
Bowen ratio		0.50	0.82	0.90	1.13
3) Surface to θ-Minimum					
θ Minimum (P*)	0.15	0.35	0.55	0.40	0.10
$\Delta\theta$ (^oK)	1.6	1.6	1.7	1.3	1.4
Δr (gm kg^{-1})	1.3	1.3	1.6	1.4	1.2
Bowen ratio	0.50	0.50	0.44	0.38	0.48
4) Surface to Mean $\tilde{\theta}$, $\tilde{r}$					
$\Delta\theta$ (^oK)	1.1	1.4	1.4	1.1	1.3
Δr (gm kg^{-1})	1.4	1.4	1.3	1.4	1.5
Bowen ratio	0.32	0.41	0.44	0.32	0.35

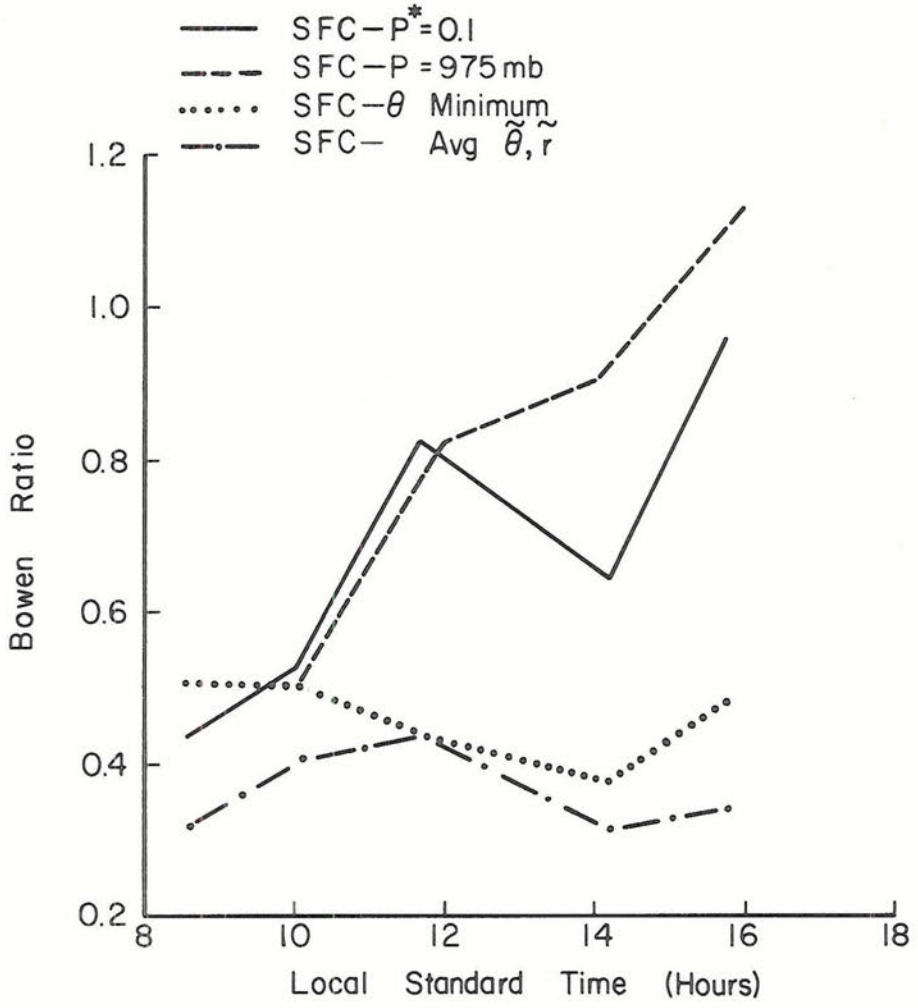

Figure 3.25: The time variation of the Bowen ratio computed using $\tilde{\theta}$, and $\tilde{r}$ differences between the surface and selected levels in the dry convective layer.

Qualitatively, the ratio might be expected to be relatively high in the morning and to gradually decrease through the afternoon as the sensible heat flux decreases. This is the tendency shown by the Bowen ratios computed by differencing from the surface to the θ-minimum. We see that the Bowen ratio differs markedly depending on the choice of θ_t, r_t. Current parameterization models for the sub-cloud layer are using method four above: on average, this gives the lowest Bowen ratio for these data. This clearly needs further study.

4. THE MODIFICATION OF THE LOWER ATMOSPHERE BY PRECIPITATING CONVECTION

4.1 Data Used

Although precipitating convection and the cloud layer itself is outside the main area of this study, the modification of the lower atmosphere, initially the sub-cloud layer, by precipitating convection will be discussed. The data used in this section is a set of 22 category IV (heavy rain) soundings which were taken before precipitation began and again after precipitating ended for eleven heavy precipitation events. Average pre- and post-precipitation soundings were produced from the eleven pairs of soundings mentioned above. Average r-, θ-, θ_e- and θ_{es}-profiles were computed (Figures 4.1, 4.2, 4.3, and 4.4).

Measurements of horizontal transports are not available. This effect is assumed to be small on any given day and is, therefore, considered negligible in the profile changes which result from averaging data from many days. The changes in structure in the pre- and post-precipitation soundings will be interpreted as changes which are due to convection.

In order to test the statistical significance of the data, the standard error (standard error = standard deviation/(number of observations)$^{\frac{1}{2}}$) of the measured change in potential temperature and mixing ratio at each pressure level was computed and has been inserted into Figures 4.1 and 4.2. The standard error is generally less than the value of the difference which lends credence to the subsequent results.

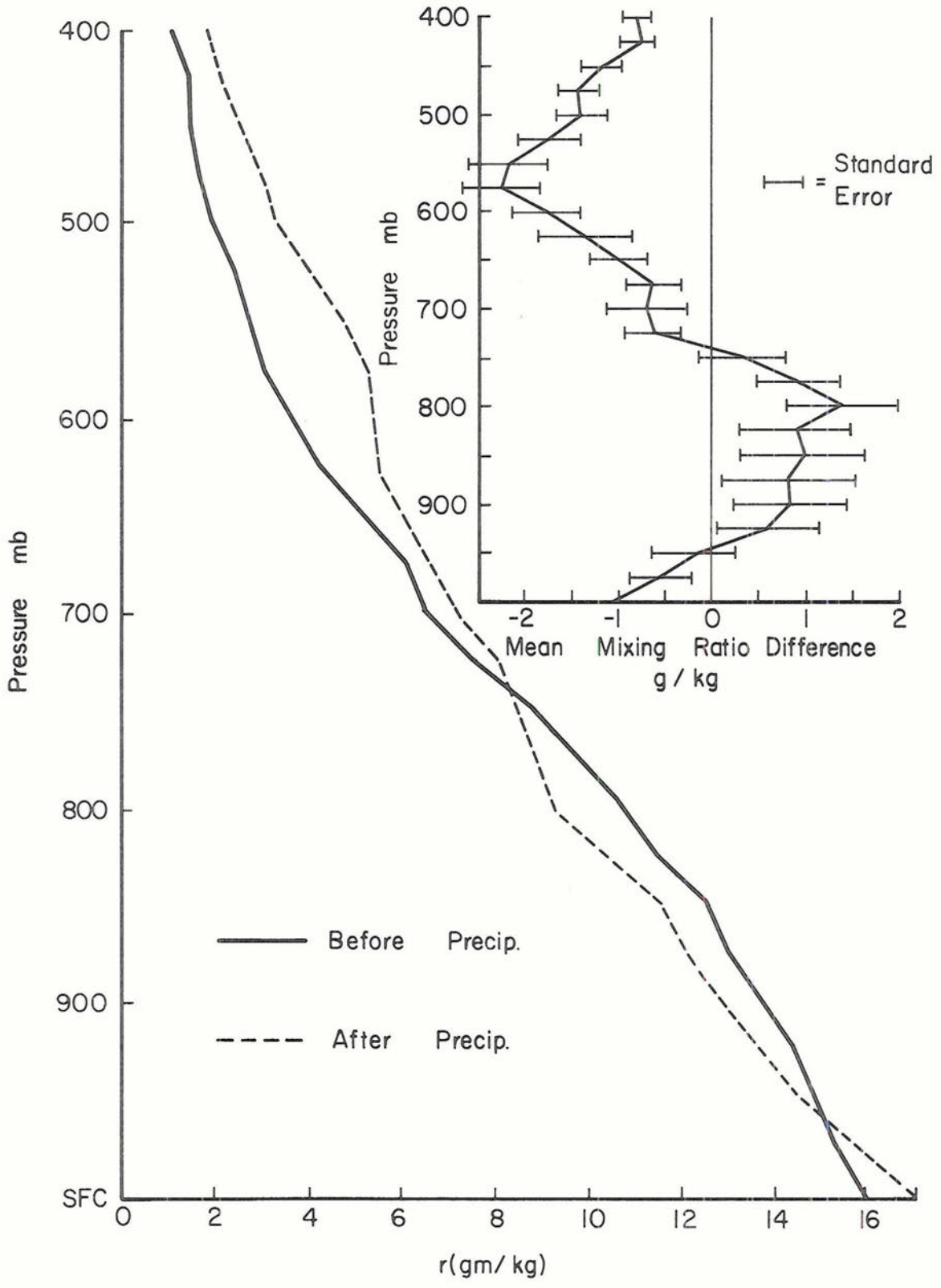
400
500
600
700
800
900
SFC
Pressure mb
0
2
4
6
8
10
12
14
16
r(gm/kg)
Before Precip.
After Precip.
Pressure mb
Standard Error
-2
-1
0
1
2
Mean Mixing Ratio Difference
g / kg

Figure 4.1

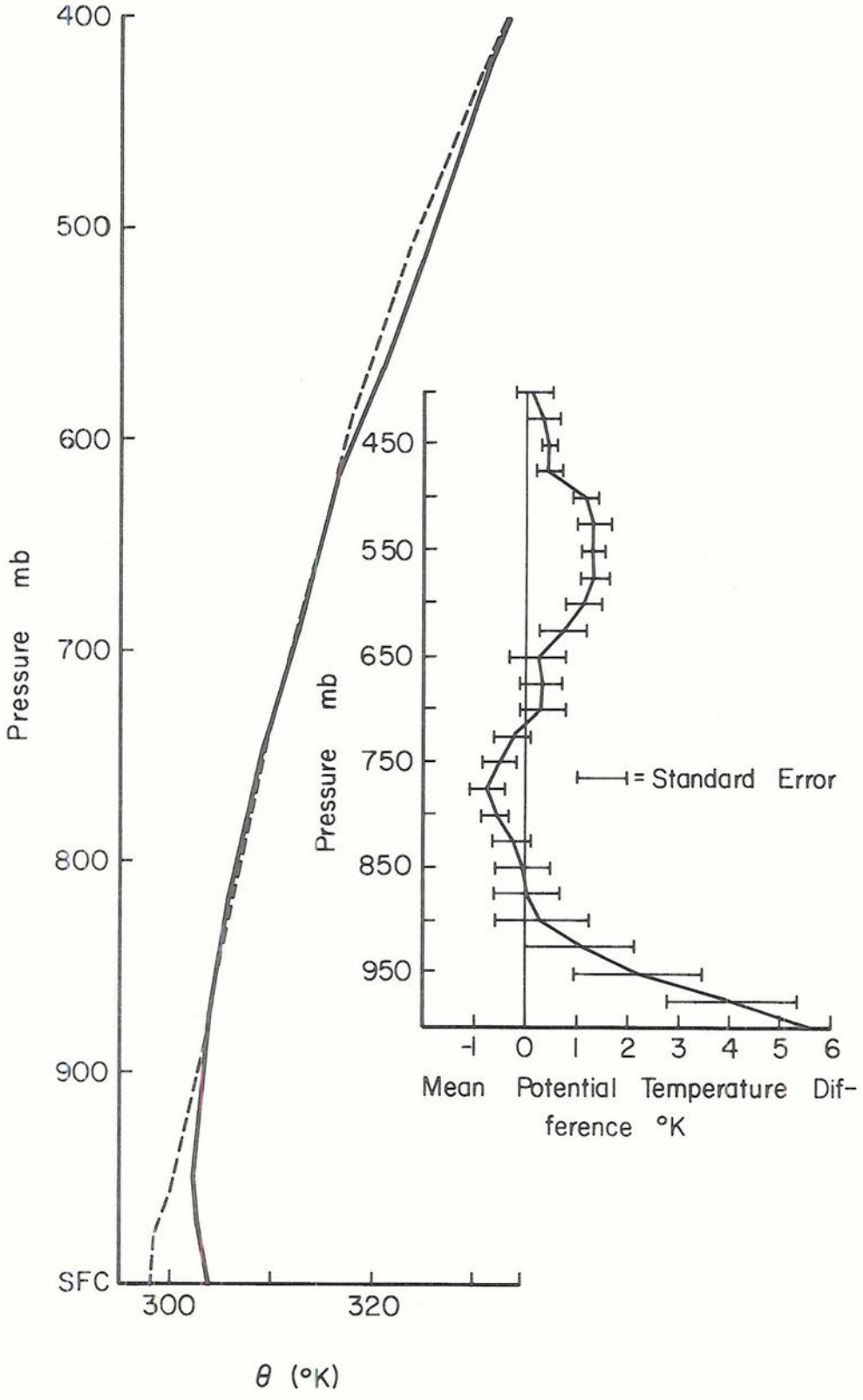
400
500
600
700
800
900
SFC
Pressure mb
300
320
θ (°K)
450
550
650
750
850
950
Pressure mb
= Standard Error
-1
0
1
2
3
4
5
6
Mean Potential Temperature Difference °K

Figure 4.2

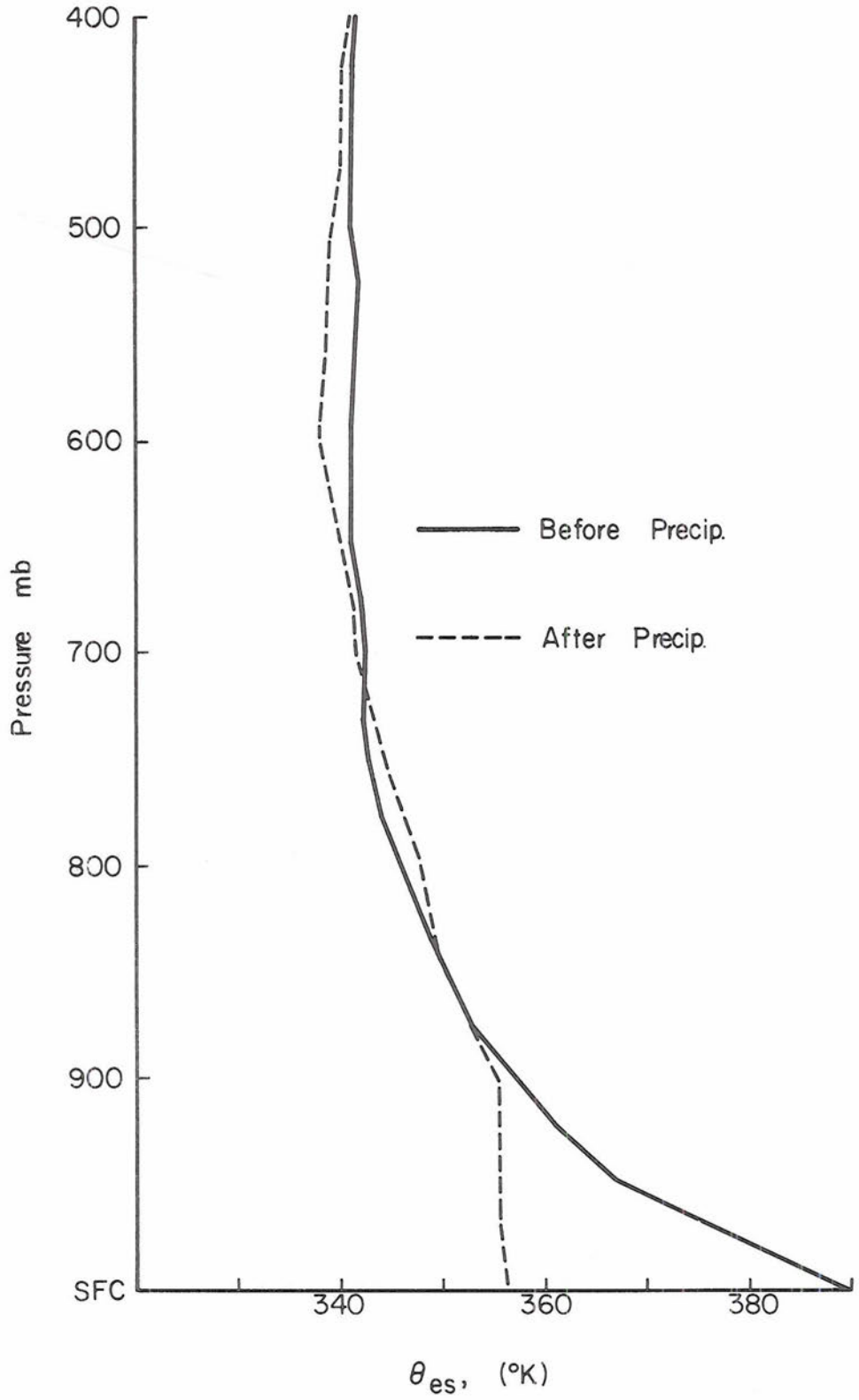
400
500
600
700
800
900
SFC
Pressure mb
340
360
380
θ_{es}, (°K)
Before Precip.
After Precip.

Figure 4.3

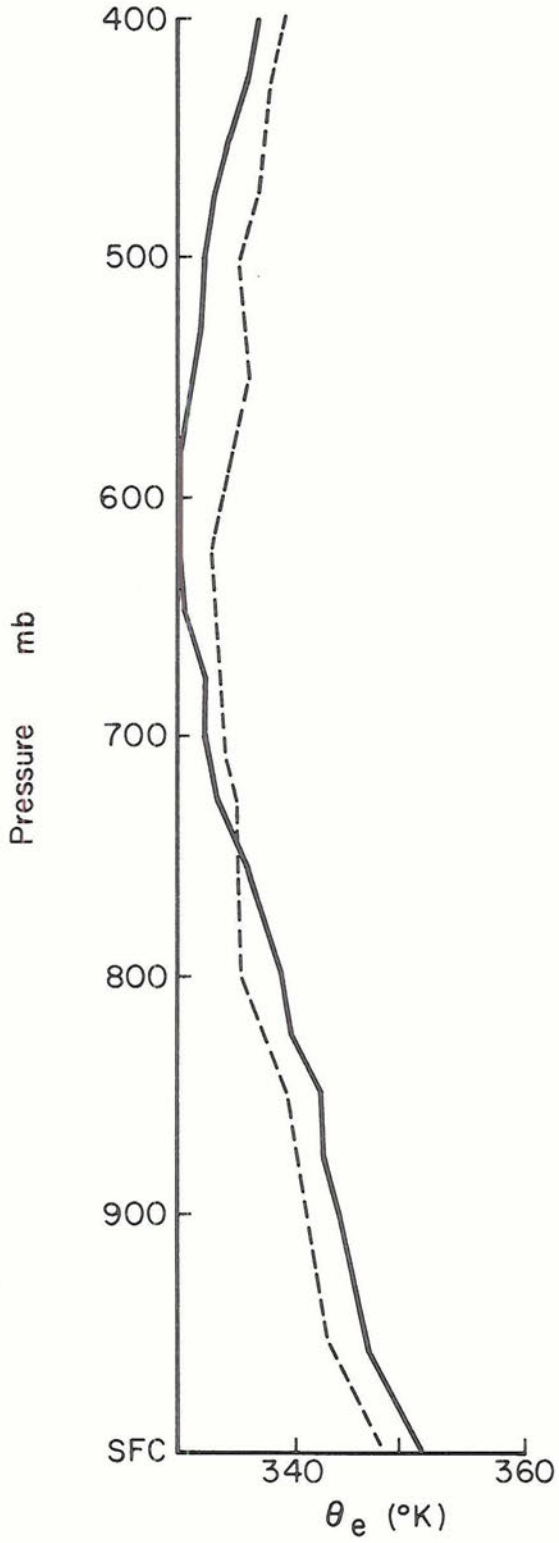

Figure 4.4

4.2 Mixing Ratio (Figure 4.1)

There is little ambiguity in the changes which are observed in the moisture structure. The layer between the surface and about 960 mb. has increased its moisture content. From 960 to 740 mb. the atmosphere has become drier by 0.5 to 1.4 gm kg^{-1}. Above 740 mb. moisture has been increased. The largest change in moisture is the increase of 1.5 to 2.0 gm kg^{-1} which occurs between 525 and 600 mb.

These changes in water vapor content are related to the liquid water transports which occur during precipitating convection. Vapor condenses, is transported vertically by the convective cells, with some of the liquid water falling out as precipitation, and subsequently re-evaporates. The moisture increase in the layer just above the surface is due, in large part, to the re-evaporation of precipitation from the surface. The moisture decrease from 940-740 mb. is due to the transport of vapor out of this layer by updraft and downdraft circulations.

The total precipitable water in the surface -150 mb. column increases from 4.6 gm before precipitation to 4.9 gm afterwards, indicating a convergence of moisture into the column.

4.3 Potential Temperature (Figure 4.2)

There is a definite cooling below 900 mb. and aloft between 650-425 mb. A slight warming is observed between 850-725 mb.

The large cooling near the surface (5-6^{o} K) reflects the evaporation of precipitation falling through the sub-cloud layer as well as the convectively induced downdrafts of cooler air.

The changes in the θ-profile represent changes in the stability of the atmosphere. Precipitating convection acts to stabilize the initially unstable layer below 950 mb. (i.e., the surface super-adiabatic layer). In fact, the entire layer below 725 mb. is much more stable after precipitation than it was before. A slight destabilization is seen between 650 and 400 mb.

By the time precipitation usually ends, the amount of solar heating that is occurring is insufficient to restore the temperature profile to its original state.

4.4 Saturation Equivalent Potential Temperature (Figure 4.3)

Since potential temperature and saturation equivalent potential temperature are both functions of temperature and pressure only, a change in temperature at a specified pressure level can be expected to produce similar changes in θ_{es} and θ. In fact, examination of Figures 4.2 and 4.3 shows that the changes in θ_{es} are an amplification of the changes in θ. What has been said about the changes in the environmental θ-profiles applies equally to the θ_{es}-profiles. The value of the θ_{es} plots is that the layers in which warming and cooling occurs are more apparent. More important, it can also be seen that the environment below 900 mb. approaches a constant θ_{es}-profile after precipitation has occurred.

4.5 Equivalent Potential Temperature (Figure 4.4)

The equivalent potential temperature of a parcel of air is clearly related to the quantity $gz + c_pT + Lr$, the moist static energy, of the parcel (Madden and Robitaille, 1970). It is conserved during parcel ascent under both dry adiabatic and pseudo-adiabatic

assumptions. The changes in the vertical θ_e-profile are related to the changes in the θ and r structures which have already been discussed.

Figure 4.4 shows a uniform 2-4^o K decrease in θ_e below 750 mb. and a 1.5-5^o K increase above 750 mb. The observed decrease results from a sinking of air in downdrafts from higher levels, where θ_e is lower.

The structural changes above 750 mb. result from the transport of high θ_e air from near the surface into the middle troposphere probably by the decay of cumulus towers. This air (which is also very moist) mixes with the relatively low θ_e air aloft causing a net increase in θ_e (and moisture content).

In terms of moist static energy, Figure 4.4 is evidence that strong convection acts to transport energy upward, which should not be surprising. Comparison with Figure 4.1 indicates that a large part of this energy is in the form of latent heat.

Precipitating convection is also seen to reduce the vertical variation of θ_e and to cause the level of minimum θ_e to be displaced and downward 10-15 mb.

Perhaps the most dramatic change is that in the stability of the lower atmosphere before and after precipitation. Figure 4.5 shows the θ_{es}- and θ_e-profiles before and after precipitation. A surface parcel displaced upward before precipitation is positively buoyant up to the LCL which is located slightly below the level of free convection (LFC) (i.e., the level above which the moist parcel is unstable with respect to its environment and will proceed upward

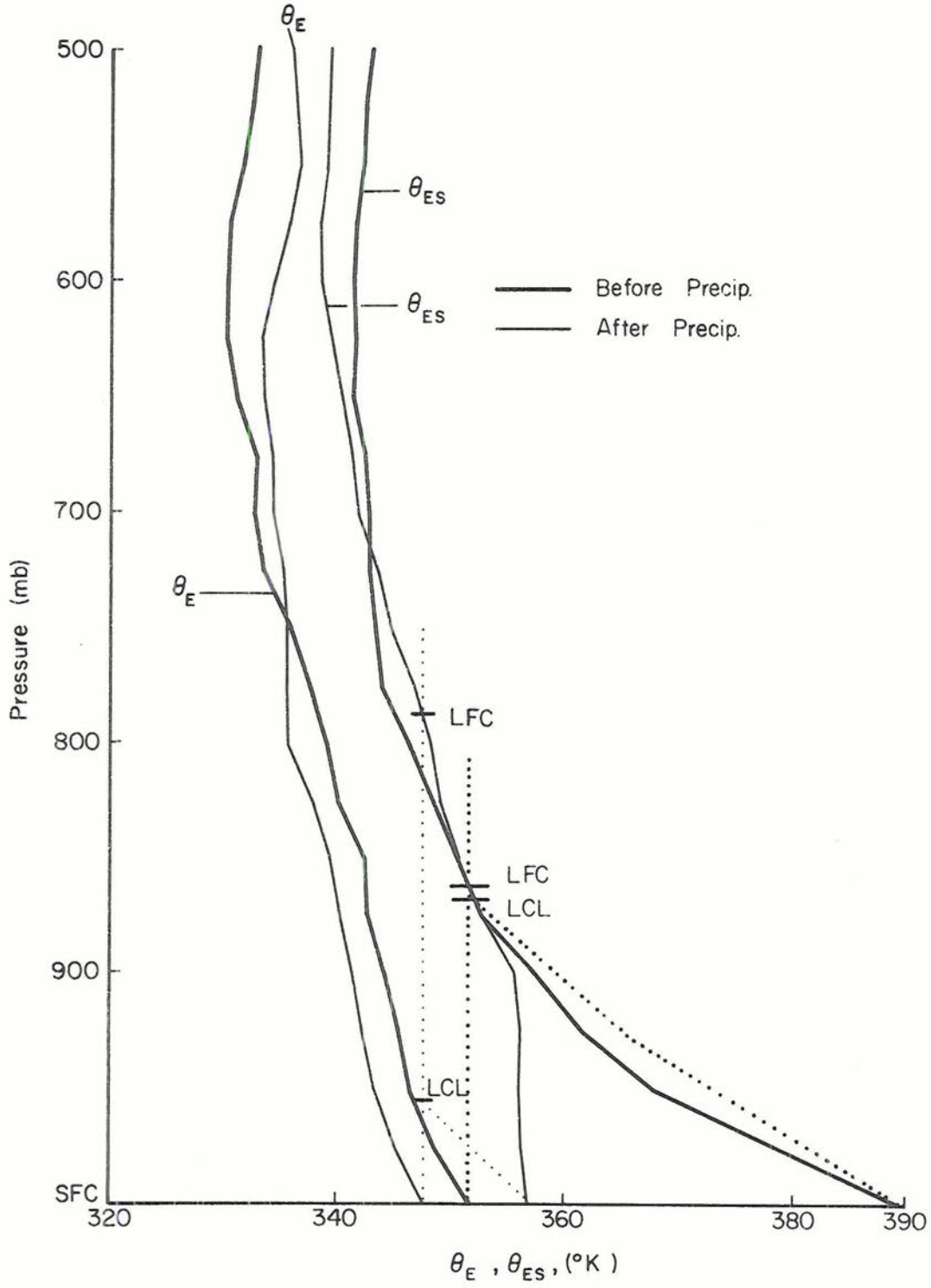

Figure 4.5: θ_e- and θ_{es}-profiles before and after precipitation. Changes in atmospheric stability are indicated by the change in the height of the lifting condensation level (L.C.L.) and the level of free convection (L.F.C.) before and after precipitation.

without added impulse). In comparison, a parcel displaced upward from the surface after precipitation is stable and remains stable above the LCL; necessitating a forced lifting through about 200 mb. for deep convection to occur.

5. SUMMARY AND CONCLUSIONS

A large sample of data collected primarily for the study of convection has been used to obtain some insight into dry convection in the atmosphere. VIMHEX II was unique in that it was one of the first major land experiments during which the new VIZ-NWS radiosonde was used.

A great deal of care was taken during the processing of the data and considerable attention paid to the effect of different averaging techniques on the mean profiles that were obtained. It was found that in order to study specific structural features specially selected data had to be used. Without the selections of data that were made it is doubtful that any meaningful results could have been obtained.

Out of necessity a method of determing the LCL which corresponds to the top of the dry convective layer was developed. The LCL's computed by this method were shown to agree well with the observed cloudbase. There was evidence in the LCL vertical structure that air going into cloud slopes upward from the surface rather than rising vertically. This feature allowed an estimation of the accuracy of the radiosonde humidity measurements and the amount of thermal lag inherent in the hygristor. The humidity measurements were determined to be accurate to within 2% of the true value, except near saturation. The hygristor was found to have a thermal lag of about 10 seconds in the dry convective layer.

The mean profiles that were computed indicate a rather complex structure in the dry convective layer. The most interesting result was the discovery that the lower portion of what has been called the

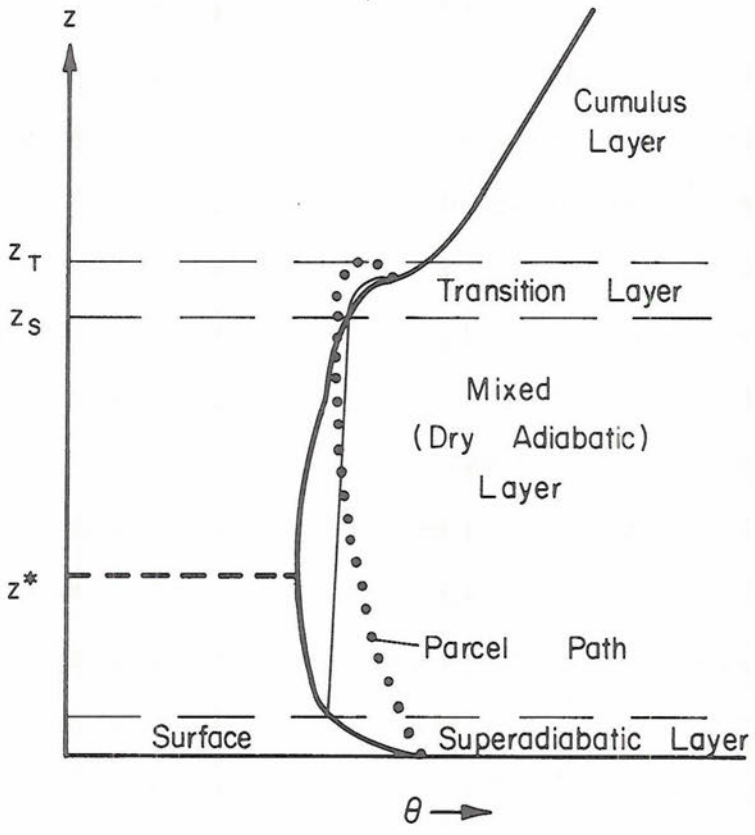

Figure 5.1: Modification of model sub-cloud structure suggested by VIMHEX II data.

"constant θ" layer is, in fact, slightly unstable during most of the convective period. The modification of the model sub-cloud structure (Figure 3.1) which the VIMHEX II data suggests is shown on Figure 5.1. The z* level (see Figure 5.1) is that of the θ-minimum. The significance of this feature is shown when energy flux computations are compared the measured energy flux into the layer. Some agreement is found only when the flux computations are based on the energy gradient through the entire unstable layer rather than through a fixed layer above the surface.

The time dependence of the major structural features of dry convection has been studied and a clearer picture of the development of a dry convective layer has been obtained.

The atmospheric structure below cloud has been presented, and compared with the corresponding structure of the atmosphere between clouds. Air ascending through cloudbase has been shown to have essentially "mixed" layer properties, although cloudbase air is usually slightly moister than the air found beneath it in the subcloud layer. Between the clouds, a stable transition layer is visible on many soundings.

Section 4 has presented the transformation of the dry layer by precipitation showing the dramatic stabilization, caused by the low level cooling and the simultaneous reduction in equivalent potential temperature by deep convective downdrafts.

REFERENCES

Augstein, E., 1972: Investigations of the structure and the energy budget of the low trade wind regime. Ber. Inst. Radiomet., maritime Met. University of Hamburg, 19.

Ball, F. K., 1960: Control of inversion height by surface heating. Quart. J. R. Met. Soc., 86, pp. 483.

Betts, A. K., 1970: Cumulus Convection. unpublished Ph.D. thesis, Imperial College, University of London.

Betts, A. K., 1973: Non-precipitating cumulus convection and its parameterization, Quart. J. R. Met. Soc., 99, pp. 178-196.

Betts, A. K., and F. J. Dugan, 1972: Empirical formula for saturation pseudoadiabats and saturation equivalent potential temperature. J. Appl. Meteor., 12, pp. 731-732.

Carson, D. J., 1971: On the thickness of the planetary boundary layer in diabatic conditions. Unpublished Meteorological Report, Turbulence and Diffusion Notes No. 18.

Compendium of Meteorology, 1951, Waverly Press, Boston, Massachusetts, pp. 1208-1210.

Friedman, M., 1972: A new radiosonde case: the problem and the solution. Bull. Amer. Meteor. Soc., 53, pp. 884-887.

Grant, D. R., 1965: Some aspects of convection as measured from aircraft. Quart. J. R. Meteor. Soc., 91, pp. 268-281.

Holland, J. Z., and E. M. Rasmusson, 1973: Measurements of the atmospheric mass, energy and momentum budgets over a 500-kilometer square of tropical ocean. Mon. Wea. Rev., 101, pp. 44-55.

Konrad, T. G., 1970: The dynamics of the convective process in clear air as seen by radar. J. Atmos. Sci., 27, pp. 1138-1147.

Madden, R. A., and F. E. Robitaille, 1970: A comparison of the equivalent potential temperature and the static energy. J. Atmos. Sci., 27, pp. 327-329.

Morrissey, J. F., and F. J. Brousaides, 1970: Temperature induced errors in the ML-476 humidity data. J. Appl. Meteor., 9, pp. 805-808.

Namias, J., 1940: Air mass and isentropic analysis. Amer. Meteor. Soc., fifth edition, pp. 7-8.

Ostapoff, F., W. W. Shinners, and E. Augstein, 1970: Some tests on the radiosonde humidity error. NOAA Tech. Report ERL 195-AOML 4.

REFERENCES - Continued

Riehl, H. and A. K. Betts, 1972: Humidity observations with the 1972 radiosonde instrument. Bull. Amer. Meteor. Soc., 53, pp. 887-888.

Teweles, S., 1970: A spurious diurnal variation in radiosonde humidity records. Bull. Amer. Meteor. Soc., 51, pp. 836-840.

Vul'fson, N. I., 1961: Some results of the study of convective activity in the free atmosphere. Studies of Clouds, Precipitation and Thunderstorm Electricity, Amer. Meteor. Soc., Boston, pp. 119-131.

Warner, J. and J. W. Telford, 1967: Convection below cloudbase. J. Atmos. Sci., 24, pp. 374-382.

Appendix A: Computation of Thermodynamic Variables

The basic set of thermodynamic data consists of the temperature (T) and relative humidity (RH) measurements taken at specified pressure (P) levels by radiosonde. The accuracy of the humidity data are discussed in Section 2.3.2.

Several thermodynamic variables have been computed from the basic data. These are water vapor mixing ratio (r), potential temperature (θ), saturation equivalent potential temperature (θ_{es}), and equivalent potential temperature (θ_e).

Mixing Ratio (r) has been computed using:

$$r = \varepsilon \left(\frac{e}{P-e}\right) \tag{A.1}$$

where ε = the ratio of the mean molecular weight of water vapor to that of dry air = 0.622

e = vapor pressure (mb.) and is given by the empirical formula:

$$e = .0611RH \times 10^{\left(\frac{7.5T}{T + 237.3}\right)} \qquad (T \text{ in } {}^{o}C,\ RH \text{ in } \%) \tag{A.2}$$

e_s = saturation vapor pressure and is given by:

$$e_s = 6.11 \times 10^{\left(\frac{7.5T}{T + 237.3}\right)} \qquad (T \text{ in } {}^{o}C) \tag{A.3}$$

Allowing computation of saturation mixing ratio (r_s):

$$r_s = \varepsilon \frac{e_s}{P-e_s} \tag{A.4}$$

Potential Temperature (θ) is computed from its definition

$$\theta = T \left(\frac{1000}{P}\right)^{R/C_p} \tag{A.5}$$

where R = dry gas constant = 2.871×10^{6} erg $g^{-1}\ {}^{o}K^{-1}$

C_p = specific heat of dry air = .240 IT cal $g^{-1}\ {}^{o}K^{-1}$

Saturation Equivalent Potential Temperature (θ_{es}). The formula which is generally written for saturation equivalent potential temperature is:

$$\theta_{es} = \theta \exp \frac{L_v r_s}{C_p T} \qquad (A.6)$$

The equation is obtained through integration of the entropy equation which describes the water saturation adiabatic process. One form of the entropy equation defining water saturation adiabats is:

$$C_{pm} \frac{dT}{T} - R_m \frac{dP}{P} + L_v \frac{dq_s}{T} = 0 \qquad \text{(Betts, 1973)} \qquad (A.7)$$

where R_m, C_{pm} = gas constant and specific heat of the moist air respectively

L_v = latent heat of vaporization

q_s = saturation specific humidity

The integration of (A.7) to obtain (A.6) involves several approximations, one of which is the neglect of the variation of T in the third term of (A.7). It has been shown (Betts and Dugan, 1972) that more accurate values of θ_{es} can be generated by using an empirical formula.

$$\theta_{es} = \theta \exp \left(\frac{A r_s}{T}\right) \qquad (A.8)$$

where A is empirically determined to be given by:

$$A = 2.61 + 0.0014\, \theta_w \qquad (A.9)$$

θ_w = wet-bulb potential temperature in ^oC

Since the range of θ_w is small for the data under consideration, an average value, $\theta_w \sim 20^o$ C, was used in the computations and θ_{es} was computed accoding to:

$$\theta_{es} = \theta \exp \frac{2.64\, r_s}{T} \qquad (A.10)$$

Equivalent Potential Temperature (θ_e): The equivalent potential temperature of an unsaturated air parcel is determined from (A.10) by replacing r_s by r.

$$\theta_e = \theta \exp \frac{2.64\ r}{T_{LCL}} \qquad \text{(A.11)}$$

The temperature used in (A.11) must be the temperature at which the latent heat represented by r begins to be realized, i.e., the temperature at which condensation begins or the temperature at the lifting condensation level (LCL).

LCL Computation. The LCL has been computed using the following scheme:

Given P, T, r and θ

1. Determine vapor pressure, e, from $e = \frac{Pr}{\varepsilon + r}$ (A.12)
2. From (A.3) dewpoint, T_D, can be determined

$$T_D = \frac{((237.3 * \log (e)/2.302585) - 186.527)}{(8.286 - (\log (e)/2.302585))} \qquad \text{(A.13)}$$

3. Let $\Delta T = T - T_D$ (A.14)
4. Compute an approximate average temperature, T*, in the sub-LCL layer using

$$T^* = T_D - 0.62\ \Delta T + 273.2 \quad (^oK) \qquad \text{(A.15)}$$

5. Compute a mean dewpoint lapse rate, Γ_D, below the LCL from

$$\Gamma_D = \frac{g}{\varepsilon L}\ T^* \qquad \text{(A.16)}$$

6. The LCL height, H_{LCL}, is then given by

$$H_{LCL} = \Delta T/(9.76 - \Gamma_D) \quad (km) \qquad \text{(A.17)}$$

and the temperature at the LCL, T_{LCL}, by

$$T_{LCL} = T - 9.76\ H_{LCL} + 273.2 \quad (^oK) \qquad \text{(A.18)}$$

BIBLIOGRAPHIC DATA SHEET	1. Report No. CSU-ATSP-205	2.	3. Recipient's Accession No.

4. Title and Subtitle
The Thermodynamic Structure of the Cumulus Sub-Cloud Layer

5. Report Date
August, 1973

6.

7. Author(s)
Frank J. Dugan

8. Performing Organization Rept. No. CSU-ATSP-205

9. Performing Organization Name and Address
Department of Atmospheric Science
Foothills Campus
Colorado State University
Fort Collins, Colorado 80521

10. Project/Task/Work Unit No.

11. Contract/Grant No.
NSF GA-33182

12. Sponsoring Organization Name and Address
Atmospheric Sciences Section
National Science Foundation
Washington, D. C.

13. Type of Report & Period Covered
M.S. Thesis

14.

15. Supplementary Notes

16. Abstracts

Data acquired during the 1972 Venezuelan International Meteorological and Hydrological Experiment is used to study the thermodynamic structure of the cumulus sub-cloud layer: its time dependence, and transformation by precipitation. A close relationship between lifting condensation level (LCL) and cloud base, and between LCL and the transition layer is found. Cloud "roots" in the sub-cloud layer are identified, and the improved accuracy of the 1972 VIZ-NWS radiosonde is confirmed. Different averaging techniques are used to show the diurnal dependence of the sub-cloud layer structure. A deep slightly superadiabatic layer is found. The validity of determining surface fluxes from bulk aerodynamic formulae using the difference between surface and sub-cloud layer mean quantities is questioned. The transformation of the sub-cloud layer by precipitation is presented.

17. Key Words and Document Analysis. 17a. Descriptors

Sub-cloud layer
Cumulus Convection
Dry Convection
Boundary Layer

17b. Identifiers/Open-Ended Terms

17c. COSATI Field/Group

18. Availability Statement	19. Security Class (This Report) UNCLASSIFIED	21. No. of Pages
	20. Security Class (This Page UNCLASSIFIED	22. Price